

The U(1) Gross-Neveu Model at Non-Zero Chemical Potential

Simon Hands

*Department of Physics, University of Wales, Swansea,
Singleton Park, Swansea, SA2 8PP, U.K.*

Seyong Kim

*School of Physics, High Energy Physics Division
Argonne National Laboratory
9700 S. Cass Avenue, Argonne, IL 60439*

John B. Kogut

*Department of Physics, University of Illinois at Urbana-Champaign
1110 West Green Street, Urbana, IL 61801-3080*

Abstract

The four-fermi model with continuous chiral symmetry is studied in three dimensions at non-zero chemical potential μ using both the $1/N_f$ expansion and computer simulations. For strong coupling this model spontaneously breaks its U(1) chiral symmetry at zero chemical potential and the Goldstone mechanism is realized through massless pions. The computer simulation predicts a critical chemical potential μ_c close to the lightest fermion mass in the model. As μ is increased beyond μ_c , the pion screening mass increases rapidly from zero to a nonvanishing value indicating symmetry restoration. Some lessons are drawn relevant to lattice QCD simulations at non-zero μ .

11.10.Kk, 11.15.Ha, 11.15.Pg, 11.10.Wx

Typeset using REVTeX

I. INTRODUCTION

Simulations of lattice QCD at non-zero chemical potential μ have remained in a quagmire for over a decade [1]. The lattice action becomes complex when μ is taken non-zero, so conventional computer simulation algorithms which are based on a probability distribution do not apply. The quenched version of lattice QCD, which attempts to skirt the issue by replacing the complex fermion determinant by unity, appears to be pathological in the chiral limit [2] [3]. When the bare quark mass is non-zero so the pion is not massless, one finds that quenched simulations of lattice QCD work for μ outside a “forbidden” region extending from $m_\pi/2$ to $m_B/3$, where $m_{\pi,B}$ denote pion and baryon masses respectively [4]. The failure of the quenched version of QCD to describe the forbidden region is poorly understood [5] [6] [7]. Studies of zero dimensional models of non-zero chemical potential have not been decisive – some models work in their quenched versions [8] and others do not [9]. Since such models cannot respect the Goldstone mechanism, their relevance to QCD is questionable at best.

In this paper, we study the N_f -flavor four-fermi model with U(1) chiral symmetry, sometimes called the Gross-Neveu model [10], in three dimensions (ie. two space and one time) as a function of chemical potential μ . The action is

$$\mathcal{L} = \bar{\psi}_i(\not{\partial} + \mu\gamma_0 + m)\psi_i - \frac{g^2}{2N_f}[(\bar{\psi}_i\psi_i)^2 - (\bar{\psi}_i\gamma_5\psi_i)^2], \quad (1.1)$$

where $\psi, \bar{\psi}$ are four component spinors and a sum on $i = 1, \dots, N_f$ is understood. For $\mu < \mu_c$ this model has a massless pion in the chiral limit $m \rightarrow 0$ [11] and can be studied by the leading order $1/N_f$ expansion [12] [13] as well as by conventional computer simulations. Since the pathologies in QCD simulations are tied to m_π , we can address the possibility that the presence of this massless mode is the culprit in past failures. In addition, the model has composite mesons like QCD and has sensible infra-red and ultra-violet properties. The zero chemical potential model has a chiral transition as a function of its bare coupling which can be analyzed using the $1/N_f$ expansion [14] [15]. The second order phase transition

coincides with a renormalization group fixed point and defines an interacting continuum field theory [12] [14]. It will prove interesting to simulate the U(1) four-fermi model to see the physics of chiral symmetry restoration at work in a model with a realistic, composite pion. The four-fermi model lacks two central features of QCD: 1. the model does not confine, and 2. its fermion determinant is real and non-negative even when $\mu \neq 0$.

We shall see that the simulation study of the four-fermi model is completely successful and physical, and in agreement with the predictions of the $1/N_f$ expansion. In addition to the usual thermodynamic quantities such as the chiral condensate $\langle \bar{\psi}\psi \rangle$, the fermion energy density ϵ , and the fermion density ρ itself, we will measure some spectroscopic features of the model. These will include the pion and fermion screening lengths, since they are so closely tied to the physics issues of interest. Recall how chemical potentials are implemented and screening lengths are measured. Consider a symmetric L^3 lattice and label one of the axes τ , “temporal.” In the $+\tau$ direction assign a factor $\exp(\mu)$ to each such link in the action, and in the $-\tau$ direction assign a factor $\exp(-\mu)$. These exponential factors favor quark propagation in the $+\tau$ direction and when μ is small in units of the reciprocal lattice spacing, ie. $\mu a \rightarrow 0$, we have a useful, well-behaved transcription of the chemical potential to a discretized system [16] [17]. Screening lengths are calculated in this environment by calculating propagation with a source at $\tau_i = 0$ and a sink at $\tau_f = \tau$. The exponential fall-off with τ then gives an estimate of the appropriate screening length, as will be illustrated through detailed calculations in the text below. The simplest expectation is that the pion inverse screening length should be zero in the chiral limit for small μ where chiral symmetry is spontaneously broken, and as μ increases through a critical value μ_c , where chiral symmetry is restored, the pion inverse screening length should increase from zero non-analytically. The fermion inverse screening length should decrease linearly with μ and vanish at $\mu_c = m_f$, where m_f is the value of the fermion mass at $\mu = 0$. Interactions are expected to decrease μ_c below this free field result, but at large N_f the naive result should be accurate. The result $\mu_c = m_f$ assumes that the fundamental fermion is the lightest fermion in the model’s mass spectrum. Although this result is expected in three dimensions, it is not true in four-Fermi

models in two dimensions, where there are “kink” solutions and kink – anti-kink bound states [18]. Computer simulation of the two dimensional model were successful in finding the kink solutions and the subtle theoretical predictions were confirmed [19]. In this study we shall confirm the naive expectation $\mu_c = m_f$ with good control. In fact, the μ -dependence of the fermion screening length will be consistent with,

$$m_f(\mu) = m_f(0) - \mu \quad (\mu < \mu_c = m_f(0)) \quad (1.2)$$

which is also the free-field prediction.

The results of our $1/N_f$ calculation and lattice simulations were very clear. The simulation gave the expected physical answers for both large N_f ($N_f = 12$), and intermediate N_f ($N_f = 4$). We worked near the chiral limit and found no pathologies when μ passed through the value $m_\pi/2$. In fact, the algorithm was well-behaved for all μ and computer simulations in the immediate vicinity of $\mu_c = m_f(0)$ were only limited by finite size effects of the expected variety. The chiral symmetry restoring transition was clear in all the observables calculated and excellent consistency was found between the various measurements.

Does this success help us understand the confused state of QCD simulations at non-zero chemical potentials? It certainly indicates that a massless pion is *not* the culprit behind the failures encountered in QCD simulations. The compositeness of the pion is also seen to be harmless. As suggested by many authors in the past [1], the complex nature of the QCD fermion determinant must be the source of the problem. The quenched version of QCD ignores the complex part and possible rapid variation in the determinant and is probably pathological because of this, as illustrated in the single-site U(1) model of Gibbs [9]. A successful simulation of QCD at non-zero μ may require a wholly new algorithmic approach. The present generation of fermion algorithms calculate the fermion propagator in a given gauge field background, and this intermediate step may not yield useful results in QCD for $m_\pi/2 < \mu < m_B/3$ [4].

This paper is organized as follows. In Sec. II we define the lattice version of the U(1) four-fermi model and present some leading order large- N_f results for the first order chiral

symmetry restoring transition for $\mu > 0$ in the model, which will be compared to computer simulations later in the paper. In Sec. III we consider the computer simulations of the $N_f = 12$ and 4 models. We shall find that the usual bulk thermodynamic observables such as $\langle \bar{\psi}\psi \rangle$, energy densities and number densities successfully expose the chiral transition. In addition, spectroscopic measurements are equally clear and particularly informative. The pion inverse screening length is essentially zero in the broken, low μ phase, but is non-zero in the unbroken phase. The fermion inverse screening length decreases linearly with μ in the broken phase and vanishes at the same critical point seen in the other observables, $\mu_c \simeq m_f(0)$, the fermion mass observed at $\mu = 0$. The hybrid Monte Carlo algorithm we use is efficient for all μ and the convergence of its underlying conjugate-gradient routines to invert the lattice Dirac operator does not deteriorate with increasing μ . Sec. IV includes a brief summary and remarks on the lessons learned in this study.

II. LATTICE FORMULATION OF THE GROSS-NEVEU MODEL

The lattice action for the bosonized Gross-Neveu model with U(1) chiral symmetry is

$$S = \sum_{i=1}^{N_f/4} \left[\sum_{x,y} \bar{\chi}_i(x) \mathcal{M}_{x,y} \chi_i(y) + \frac{1}{8} \sum_x \bar{\chi}_i(x) \chi_i(x) \left(\sum_{\langle \tilde{x}, x \rangle} \sigma(\tilde{x}) + i\varepsilon(x) \sum_{\langle \tilde{x}, x \rangle} \pi(\tilde{x}) \right) \right] + \frac{N_f}{8g^2} \sum_{\tilde{x}} (\sigma^2(\tilde{x}) + \pi^2(\tilde{x})). \quad (2.1)$$

Here, χ_i and $\bar{\chi}_i$ are complex Grassmann-valued staggered fermion fields defined on the lattice sites, the auxiliary scalar and pseudoscalar fields σ and π are defined on the dual lattice sites, and the symbol $\langle \tilde{x}, x \rangle$ denotes the set of 8 dual sites \tilde{x} adjacent to the direct lattice site x . The auxiliary fields only appear to quadratic order, and can be integrated out to recover a lattice action in terms of fermion fields only (bosonization is also possible for the continuum Lagrangian (1.1)). The parameter N_f will turn out to be the number of physical fermion species described by the numerical simulation, and must be an integer multiple of 4. The fermion kinetic operator \mathcal{M} is given by

$$\mathcal{M}_{x,y} = \frac{1}{2} [\delta_{y,x+\hat{0}} e^\mu - \delta_{y,x-\hat{0}} e^{-\mu}] + \frac{1}{2} \sum_{\nu=1,2} \eta_\nu(x) [\delta_{y,x+\hat{\nu}} - \delta_{y,x-\hat{\nu}}] + m\delta_{y,x}, \quad (2.2)$$

where m is the bare fermion mass, μ is the chemical potential, and $\eta_\nu(x)$ are the Kawamoto-Smit phases $(-1)^{x_0+\dots+x_{\nu-1}}$. The symbol $\varepsilon(x)$ denotes the alternating phase $(-1)^{x_0+x_1+x_2}$.

As described in refs. [13] [14], the model (2.1) can be recast in terms of fields $q(Y)$ defined on a lattice of twice the spacing, where the field q has explicit spinor and flavor indices. In momentum space the kinetic part of the action reads

$$\begin{aligned} S_{kin} = & \sum_i \int \frac{d^3k}{(2\pi)^3} \sum_{\nu=1,2} \frac{i}{2} [\bar{q}_i(k)(\gamma_\nu \otimes \mathbb{1}_2)q_i(k) \sin 2k_\nu + \bar{q}_i(k)(\gamma_4 \otimes \tau_\nu^*)q_i(k)(1 - \cos 2k_\nu)] \\ & + \frac{1}{2} [\bar{q}_i(k)(\gamma_0 \otimes \mathbb{1}_2)q_i(k)[i \sin 2k_0 \cosh \mu + (1 + \cos 2k_0) \sinh \mu] \\ & + \bar{q}_i(k)(\gamma_4 \otimes \tau_3^*)q_i(k)[i(1 - \cos 2k_0) \cosh \mu + \sin 2k_0 \sinh \mu]] + m\bar{q}_i(k)(\mathbb{1}_4 \otimes \mathbb{1}_2)q_i(k), \end{aligned} \quad (2.3)$$

with τ_i the Pauli matrices, which act on the 2 component flavor degrees of freedom, and

$$\gamma_\nu = \begin{pmatrix} \tau_\nu & \\ & -\tau_\nu \end{pmatrix}; \quad \gamma_0 = \begin{pmatrix} \tau_3 & \\ & -\tau_3 \end{pmatrix}; \quad \gamma_4 = \begin{pmatrix} & -i\mathbb{1}_2 \\ i\mathbb{1}_2 & \end{pmatrix}; \quad \gamma_5 = \begin{pmatrix} & \mathbb{1}_2 \\ \mathbb{1}_2 & \end{pmatrix}. \quad (2.4)$$

The momentum integral extends over the range $k \in (-\pi/2, \pi/2]$. On a finite system the integral is replaced by a sum over $L/2$ modes, where L is the number of lattice spacings in a given direction. In the large wavelength limit $k \rightarrow 0$ we recover the standard Euclidean continuum form $\bar{q}_j(\not{\partial} + \mu\gamma_0 + m)q_j$, where j now runs from 1 to $N_f/2$.

The interaction part of the action can be rewritten as

$$S_{int} = \sum_Y \hat{\sigma}(\tilde{Y})\bar{q}_i(Y)(\mathbb{1}_4 \otimes \mathbb{1}_2)q_i(Y) + \hat{\pi}(\tilde{Y})\bar{q}_i(Y)(i\gamma_5 \otimes \mathbb{1}_2)q_i(Y) + O(a), \quad (2.5)$$

where $\hat{\sigma}(\tilde{Y})$, $\hat{\pi}(\tilde{Y})$ denote the sum of the eight scalar fields associated with the site Y on the blocked lattice (see [14] for full details), and a is the lattice spacing, which has been set to unity in Eqns. (2.1-3). The $O(a)$ terms are non-covariant and flavor non-singlet – if we used a formulation in which the scalar fields were defined on the direct lattice sites, then such non-covariant terms would appear at $O(a^0)$ [20].

The lattice action (2.1) has a global vector $U(N_f/4)$ symmetry

$$\chi_i \mapsto \Omega_{ij}\chi_j \quad ; \quad \bar{\chi}_i \mapsto \bar{\chi}_j\Omega_{ji}^\dagger \quad ; \quad \Omega \in U(N_f/4), \quad (2.6)$$

and, in the chiral limit $m \rightarrow 0$, a global ‘‘axial’’ $U(1)$ symmetry

$$\chi \mapsto e^{i\alpha\varepsilon(x)}\chi \ ; \ \bar{\chi} \mapsto \bar{\chi}e^{i\alpha\varepsilon(x)} \ ; \ \phi \equiv (\sigma + i\pi) \mapsto e^{-2i\alpha}\phi. \quad (2.7)$$

In the q -basis the rotation (2.7) reads:

$$q \mapsto \exp i\alpha(\gamma_5 \otimes \mathbb{1}_2)q \ ; \ \bar{q} \mapsto \bar{q} \exp i\alpha(\gamma_5 \otimes \mathbb{1}_2). \quad (2.8)$$

The $U(1)$ symmetry is spontaneously broken by the condensate $\langle \bar{\chi}\chi \rangle$ (or equivalently $\langle \sigma \rangle$): for $m \neq 0$ this direction of symmetry breaking is picked out.

The action (2.1) may be simulated using a hybrid Monte Carlo algorithm [21], in which the Grassmann fields are replaced by complex commuting pseudo-fermion fields $\psi(x)$ governed by the action

$$S = \sum_{xy} \sum_{ij=1}^{N_f/4} \frac{1}{2} \psi_i^*(x) (M^\dagger M)_{xyij}^{-1} \psi_j(y) + \frac{N_f}{8g^2} \sum_{\tilde{x}} \left(\sigma^2(\tilde{x}) + \pi^2(\tilde{x}) \right), \quad (2.9)$$

where

$$M_{xyij} = \mathcal{M}_{xy}\delta_{ij} + \delta_{xy}\delta_{ij} \frac{1}{8} \sum_{\langle \tilde{x}, x \rangle} [\sigma(\tilde{x}) + i\varepsilon(x)\pi(\tilde{x})]. \quad (2.10)$$

Integration over the ψ fields yields the functional measure $\det(M^\dagger M)$. Note that the kinetic part of M , \mathcal{M} , is strictly real even for $\mu \neq 0$, and that the complex part $\sigma + i\varepsilon\pi$ is diagonal. Thus, schematically,

$$\begin{aligned} \det(M^\dagger M) &= \det M^* \det M \\ &= \det(\mathcal{M} + \sigma + i\varepsilon\pi) \det(\mathcal{M} + \sigma - i\varepsilon\pi). \end{aligned} \quad (2.11)$$

Since each matrix \mathcal{M} effectively describes $N_f/2$ fermion species, we conclude that the hybrid Monte Carlo simulation describes a system of N_f fermion species, $N_f/2$ having positive chiral charge and $N_f/2$ negative. To be more precise, the full symmetry of the lattice model in the continuum limit is $U(N_f/2)_V \otimes U(N_f/2)_V \otimes U(1)_A$ rather than the $U(N_f)_V \otimes U(1)_A$ we would obtain if all species transformed identically with respect to chiral rotations. At non-zero lattice spacing, of course, the symmetry group is smaller as discussed above: $U(N_f/4)_V \otimes$

$U(N_f/4)_V \otimes U(1)_A$. In all cases, of course, it is the $U(1)_A$ symmetry which is broken, either spontaneously by the dynamics of the system, or explicitly by a bare fermion mass.

It was found that the performance of the hybrid Monte Carlo procedure could be optimized in two ways: firstly, as described in [13] [14], by tuning the effective number of fermion species N'_f used in the guidance part of the program (ie. during the integration of the equations of motion along a microcanonical trajectory) to maximize the acceptance rate of the Monte Carlo procedure for fixed timestep $\Delta\tau$; and secondly by choosing the trajectory length τ at random from a Poisson distribution of mean $\bar{\tau}$. This second refinement, which guarantees ergodicity, was found to dramatically decrease autocorrelation times [22].

In our specific application we found that the choice $\Delta\tau = 0.01$ was adequate – the acceptance rate in the Monte Carlo procedure was always high (better than 80%) while the algorithm sampled configuration space with good speed and efficiency. For the $N_f = 4$ model the acceptance rate was improved by taking N'_f slightly larger, typically 4.05, although the “best” choice of N'_f/N_f certainly depends on lattice sizes (16^3 in our case) and couplings ($0 \lesssim 1/g^2 \lesssim 1.0$) and bare fermion masses (0.01 in lattice units). The trajectory lengths were chosen from a Poisson distribution with $\bar{\tau}$ typically between 1 and 2. In the immediate vicinity of the critical μ , a larger $\bar{\tau}$ probably would have been better, but we had no trouble obtaining good data with modest error bars from runs of several hundred trajectories. The data and error bars will be presented in tables in the next section. We used identical parameters when the $N_f = 12$ model was simulated except N'_f was now tuned typically to 12.12, for better acceptance rates.

As well as measuring the expectation value of the scalar field $\langle\sigma\rangle$ in the simulation, which for our purposes serves as an order parameter, we also monitored the chiral condensate $\langle\bar{\chi}\chi\rangle$, the energy density $\langle\epsilon\rangle$, and the fermion number density $\langle\rho\rangle$, which are defined as follows:

$$\begin{aligned} -\langle\bar{\chi}\chi\rangle &= \frac{1}{V}\text{tr}S_F = \frac{1}{V}\langle\text{tr}M^{-1}\rangle, \\ \langle\epsilon\rangle &= -\frac{1}{V_s}\frac{\partial\ln Z}{\partial\beta} = \frac{1}{V}\text{tr}\partial_0\gamma_0 S_F = \frac{1}{2V}\langle\sum_x e^\mu M_{x,x+\hat{0}}^{-1} - e^{-\mu} M_{x,x-\hat{0}}^{-1}\rangle, \end{aligned} \quad (2.12)$$

$$\langle \rho \rangle = -\frac{1}{V_s \beta} \frac{\partial \ln Z}{\partial \mu} = \frac{1}{V} \text{tr} \gamma_0 S_F = \frac{1}{2V} \left\langle \sum_x e^\mu M_{x,x+\hat{0}}^{-1} + e^{-\mu} M_{x,x-\hat{0}}^{-1} \right\rangle.$$

Here V_s is the spatial (ie. two-dimensional) volume, β the inverse temperature, and $V = V_s \beta$ the overall volume of spacetime. The final expression in each case is the quantity measured in the simulation, using a noisy estimator to calculate the matrix inverses.

Finally, as well as results from numerical simulations, we can examine the action (2.1) using the $1/N_f$ expansion. To leading order, this corresponds to the saddle point solution of the path integral, or equivalently to mean field theory. We can solve for the expectation value of the scalar field $\langle \sigma \rangle$ using the gap equation [12] [13]:

$$\langle \sigma \rangle = -g^2 \langle \bar{\chi} \chi \rangle = \frac{g^2}{V} \text{tr} S_F. \quad (2.13)$$

To leading order the gap equation consists of a single tadpole. Using the form for the kinetic term (2.3), we solve self-consistently to get an equation for g^2 in terms of the dynamical fermion mass $m_f = \langle \sigma \rangle + m$. In the thermodynamic limit $L \rightarrow \infty$,

$$\frac{1}{g^2} = \frac{8}{2\pi^3} \frac{m_f}{m_f - m} \int_{-\pi/2}^{\pi/2} \frac{d^3 k}{\frac{1}{2} \{1 - \cos 2k_0 \cosh 2\mu - i \sin 2k_0 \sinh 2\mu\} + \sum_{\nu=1,2} \sin^2 k_\nu + m_f^2}, \quad (2.14)$$

Note that the $O(a)$ terms in the interaction (2.5) make no contribution at this order. Eqn. (2.14) can be reduced to a one-dimensional integral and then evaluated numerically in the limit $\mu \rightarrow 0$ [14]: however for $\mu \neq 0$ it is more efficient to simply evaluate the sum over lattice momenta on finite systems explicitly. Note that antiperiodic boundary conditions must be specified on the fermion fields in the timelike direction; we chose to apply periodic boundary conditions in the two spacelike ones.

In Figs. 1 - 5 we show the large- N_f predictions from Eqn. (2.14) evaluated on a 16^3 lattice. In Fig. 1 we show $\langle \sigma \rangle$ vs. $1/g^2$. We have chosen bare fermion masses of $m = 0.05, 0.01$ and 0.00 . This range of masses shows the sensitivity of the finite lattice results to m , gives the theoretically interesting chiral limit $m = 0.00$ and includes $m = 0.01$ to compare quantitatively to the simulation results obtained from the hybrid Monto Carlo algorithm at

$N_f = 12$ and $4, m = 0.01$. A chiral symmetry restoring symmetry point at $1/g_c^2$ slightly larger than 1.00 is found consistent with the critical index $\beta_{mag} = 1.0$ [14]. The curves at $m = 0.01$ and 0.05 smooth the transition out in the expected fashion. Only the $m = 0.00$ curve shows evidence of finite volume rounding (this was checked by evaluating the gap equation on larger lattices). Note that $\langle\sigma\rangle$ is also the fermion dynamical mass m_f in the chiral limit, so m_f is an equally good order parameter for the transition. Since m_f is an inverse correlation length, the critical exponent $\nu = 1.0$ follows from the figure. In Fig. 2 we show $\langle\sigma\rangle$ vs. μ for a bare coupling $1/g^2 = 0.5$ deep within the broken symmetry phase. This coupling will be simulated in the next section. We note that $\langle\sigma\rangle$ is essentially unaffected by μ until the immediate vicinity of the transition where $\langle\sigma\rangle$ jumps to zero through a first order phase transition. (Recall that in mean field theory a model can have a phase transition in a finite volume.) The rounding of the curves near $\mu = \mu_c$ is a finite volume effect. The critical μ_c is approximately 0.73 which compares rather well with the dynamical fermion mass in the chiral limit at $1/g^2 = 0.5$ and $\mu = 0.0, m_f = 0.84$, seen in Fig. 1. The discrepancy between μ_c and m_f is simply due to the discreteness of the lattice sums approximating continuum integrals. In the continuum limit $g \rightarrow g_c$ (ie. $m_f \rightarrow 0$), the discrepancy would approach zero. It is interesting to note that if the plot of m_f vs. $1/g^2$ in Fig. 1 is extrapolated back from $1/g_c^2$ using the assumption of linearity (ie. $\beta_{mag} = 1$), then the resulting m_f at $1/g^2 = 0.5$ is in much closer agreement. The $m = 0.01$ and 0.05 curves in Fig. 2 demonstrate that these bare masses do not distort the first order symmetry restoring transition significantly. Since the mass ratios m/m_f are 0.012 and 0.058, approximately, in the two cases and since the transition is strongly first order, this result is expected. In Fig. 3 we show the lattice gap equation prediction for σ vs. μ at $m = 0.01$ on a 16^3 lattice for values of $1/g^2$ ranging from 0.5 to 0.8, showing the effect of finite volume rounding becoming more pronounced as the physical lattice spacing is reduced. By $1/g^2 = 0.8$ the transition has become much less sharp. In Figs. 4 and 5 we show the fermion number density ρ and the fermion energy density ϵ plotted against μ in the chiral limit for three choices of couplings in the broken phase, $1/g^2 = 0.5, 0.7$ and 0.9 . Also shown in Fig. 4 is the expected continuum result for

fermions in the unbroken phase, $\rho = \mu^2/\pi$ (we have rescaled the numerical results for ρ and ϵ by a factor of two over the definitions (2.12)) [13]. For $1/g^2 = 0.9$ the transition is hard to identify. As we approach the bulk critical point $1/g_c^2 \approx 1.0$ on the finite system the signals of the phase transition become less and less dramatic. Larger lattices are necessary to obtain a quantitative picture of the transition when $1/g^2$ is chosen to be 0.9, close to the bulk continuum limit $1/g_c^2 \approx 1.0$.

III. SIMULATION RESULTS

We simulated both the $N_f = 12$ and $N_f = 4$ models at various couplings and chemical potentials. In all cases a 16^3 lattice was used, with a bare fermion mass $m = 0.01$. As explained above, due to fermion “doubling,” the $N_f = 12(4)$ model corresponds to $N_{f\text{latt}} = 3(1)$ lattice species. We simulated the $N_{f\text{latt}} = 3$ model because it should compare well with the results of the $1/N_f$ expansion (if its underlying assumptions hold in the model), and observables should be large with relatively modest fluctuations. The $N_{f\text{latt}} = 1$ model is interesting because it could show qualitative deviations from the large- N_f results; its observables will fluctuate more intensely and it will present a numerical challenge closer to that of two- or four-flavor QCD. The observables and measurement techniques were discussed above. They have also been used in our past studies of four-fermi models, so we refer the reader to those references rather than repeat standard material [13] [14]. The “new” measurements we have done concern the model’s spectroscopy. These observables are particularly revealing and we will discuss them at greater length.

Using point sources, we calculated the fermion propagator, $G_+(\vec{x}, t)$, with chemical potential μ and, $G_-(\vec{x}, t)$, with chemical potential $-\mu$. Then we formed a zero momentum fermion propagator

$$P_f(t) = \sum_{\vec{x}} G_+(\vec{x}, t), \tag{3.1}$$

and anti-fermion propagator

$$P_f(t) = \sum_{\vec{x}} G_-(\vec{x}, t). \quad (3.2)$$

Of course, $G_+(\vec{x}, t) = G_-(\vec{x}, t)$ for the zero chemical potential case. The composite pion and sigma propagators are,

$$P_\pi(t) = \sum_{\vec{x}} G_+(\vec{x}, t) G_-^\dagger(\vec{x}, t), \quad (3.3)$$

$$P_\sigma(t) = \sum_{\vec{x}} (-1)^{x+y} G_+(\vec{x}, t) G_-^\dagger(\vec{x}, t), \quad (3.4)$$

in analogy with the treatment using staggered fermions in four dimensions [23]. We also calculated propagators for the auxiliary fields in Eq. (2.1), π and σ ,

$$P_\pi(t) = \sum_{\vec{x}, t'} \pi(\vec{x}, t') \pi(\vec{x}, t' + t), \quad (3.5)$$

and

$$P_\sigma(t) = \sum_{\vec{x}, t'} [\sigma(\vec{x}, t') \sigma(\vec{x}, t' + t) - \bar{\sigma}^2]. \quad (3.6)$$

Here, $\bar{\sigma}^2$ is the square of the average of the σ field.

After calculating averages of the above propagators and their covariance matrices (see [23] for fitting techniques), we fit the various propagators to the following functional forms. For zero chemical potential:

$$P_f(t) = A[e^{-m_f t} - (-1)^t e^{-m_f(T-t)}], \quad (3.7)$$

where T is the temporal extent of the lattice, for the fermion and

$$P_\pi(t) = A[e^{-m_\pi t} + e^{-m_\pi(T-t)}], \quad (3.8)$$

for the auxiliary field, π . Similar functional forms are chosen for the anti-fermion and σ respectively. For the non-zero chemical potential case, we chose the forms,

$$P_f(t) = A[e^{-m_f^f t} - (-1)^t e^{-m_f^b(T-t)}] \quad (3.9)$$

$$P_\pi(t) = A[e^{-m_\pi^f t} + e^{-m_\pi^b(T-t)}]. \quad (3.10)$$

Since the meson has zero fermion number, we expect that $m_\pi^f = m_\pi^b$.

Those parameters which minimize correlated χ^2 were chosen as the best fitted values. We used the CERN mathematical library routine, MINUIT, as a minimization program. The error bars quoted refer to the necessary parameter changes for a change of χ^2 by one. Only two of our spectrum calculations yielded useful, accurate mass estimates. They were the fermion and the auxiliary field pion masses. Luckily, these are the two quantities most closely related to chiral symmetry and its restoration at non-zero chemical potential. It would have been interesting to calculate the σ mass, but the fluctuations in our limited data sets made that impossible.

Now let's turn to the data. The $N_{\text{flatt}} = 3$ data for m_f, m_π , the vacuum expectation value $\langle\sigma\rangle$, which we shall denote σ for simplicity in this section, and the action S are given in Table I for $\mu = 0$ and couplings $1/g^2$ ranging from 0.50 to 1.0. The order parameter σ and m_f are almost identical as they should be at large N_f . We show a plot of σ vs. $1/g^2$ in Fig. 6. Clearly chiral symmetry is broken for $1/g^2 \lesssim 0.90 - 1.00$. Also shown is the prediction of the lattice gap equation from Fig. 1. The agreement is $O(10\%)$ or better, and is very satisfactory. It is our first indication that the $1/N_f$ expansion is practical and obtains the correct physics of these models. We note from the table that the mass of the pion is “small” and quite insensitive to $1/g^2$. Since chiral symmetry is broken over this range of couplings, it should be that the pion's mass is nonzero only because of the explicit symmetry breaking provided by the small bare fermion mass, $m = 0.01$. We will obtain good evidence for this interpretation of the data when we consider the model at nonzero chemical potential.

We studied the model next at $1/g^2 = 0.50$ as a function of μ to see how a nonzero chemical potential restores chiral symmetry at a critical point. $1/g^2 = 0.50$ is a good place to look first because it is deep in the broken symmetry phase, but not too far from the bulk critical point $1/g^2 \approx 1.00$. As long as $1/g^2 \approx 0.50$ is in the scaling window of the critical point we can extract continuum physics from these simulations by standard methods. Our goals here are more modest – we wish to turn up μ and see if the conventional picture of symmetry restoration emerges. The simulation data for $1/g^2 = 0.50$ and μ ranging from

0.50 to 0.85 is given in Table II. The table includes data for m_f (the fermion mass), m_π (the pion mass), ρ (the fermion number density), σ (the vacuum expectation value of the σ field), S (the action), and ϵ (the energy density). Since the fermion mass at $\mu = 0.0$ is $m_f = 0.746(2)$ according to Table I, we expect naively a chiral symmetry restoring transition at $\mu_c = 0.746(2)$. This result is beautifully reproduced by the simulation. In Fig. 7 we plot the order parameter σ vs. μ for fixed $1/g^2 = 0.50$, and we see restoration of the symmetry at $\mu_c = 0.725(25)$. The curve is very abrupt and we suspect, naturally, that a simulation on a larger lattice at smaller bare fermion mass m would show a first order discontinuous transition. The curve is also quantitatively very similar to the predictions of the lattice gap equation which is also shown – once again, the discrepancy is $O(10\%)$ and may presumably be ascribed to $O(1/N_f)$ corrections.

As discussed in the introduction, one of the purposes of studying this model was to verify that the lattice formulation, given a proven algorithm, obtains the correct physics at non-zero chemical potential even in a model with a Goldstone pion. Quenched QCD simulations have pathologies when μ approaches $m_\pi/2$, and although the chiral restoring transition is expected at $\mu_c = m_B/3$, one-third the mass of the nucleon, there is little numerical evidence for this [2] [3] [4]. Many reasons have been proposed in hindsight for this catastrophe and several of them hinge on the presence of a Goldstone pion in the theory's spectrum. In the simulations here $m_\pi/2 \approx 0.09$ while the expected transition is at $\mu_c = m_f = 0.74(2)$. In QCD simulations the two mass scales, $m_\pi/2$ and $m_B/3$, are actually quite close in numerical simulations performed to date, and this has further clouded the situation. In our U(1) four-fermi model, we can simulate the model very close to the chiral limit in the sense that the explicit breaking is much smaller than the dynamical breaking (ie. bare mass $m \ll m_f$, the dynamical mass). Fig. 7 and the rest of the data in Table II show that $m_\pi/2$ is not a point of any special significance and the simulation algorithm gives the expected $\mu_c = 0.74(2)$ nicely. Additional simulations show that the value $m = 0.01$ is not crucial to these conclusions, and the chiral limit $m \rightarrow 0$ does not contain surprises even when $\mu \neq 0$. For example, in Fig. 8 we show σ vs. m for $1/g^2 = 0.50$ and $\mu = 0.50$. Unlike the tortuous situation in quenched

QCD where plots of $\langle \bar{\psi}\psi \rangle$ vs. m have strong downward curvature for $\mu \gtrsim m_\pi/2$ [1], the extrapolation to the chiral limit here is essentially linear and without surprises. Simulations at larger values of m would have been as clear as the $m = 0.01$ case studied here in detail.

The transition at $\mu_c = 0.74(2)$ is seen equally well in the fermion number and energy densities (Fig. 9), and the action itself (Fig. 10). These curves compare well with the analytic large- N_f results presented in Sec. II above. The spectroscopy of the model and its dependence on μ is particularly interesting. A recent study of quenched QCD [4] showed that in the limited range $0 < \mu < m_\pi/2$, the baryon mass as defined through the exponential falloff of a Euclidean propagator as in Eq. (3.7) decreased linearly with μ and would vanish by linear extrapolation at $\mu_c = m_B/3$ as expected. Unfortunately, the quenched simulation algorithm suffers from slow convergence and large fluctuations for $\mu \gtrsim m_\pi/2$, so nothing is known quantitatively in the “forbidden” region, $m_\pi/2 < \mu < m_B/3$. In addition, the quenched QCD simulation showed that the pion mass, as defined through the exponential fall-off of a propagator as in Eq. (3.8), is insensitive to μ for $\mu \lesssim m_\pi/2$. This is another sensible result which could not be confirmed at larger μ due to the pathologies of the quenched simulation. In our four-fermi model the analogous calculations are successful for all μ . In Fig. 11 we show the fermion mass as obtained from Eq. (3.7). Up to modest and expected finite size effects which reduce the fermion mass estimates in the vicinity of μ_c , the calculation is successful, and gives a critical chemical potential near $0.74(2)$, although larger lattice studies and a systematic analysis of finite size effects would be necessary to obtain a quantitative prediction. Also in Fig. 11 we show the pion mass m_π , calculated using Eq. (3.8), as a function of μ . The pion mass exhibits no μ dependence until we reach the vicinity of $\mu_c = 0.74(2)$ where it jumps up indicating chiral symmetry restoration. We wanted to measure the σ mass over the same range, but its propagator was noisier than the pions and quantitative estimates were not achieved. We had hoped to verify that the pion and the sigma are degenerate and heavy for $\mu > 0.74(2)$, indicating chiral symmetry restoration. Although from this perspective our calculations were only partially successful,

they gave decisive physical answers expected of a Goldstone particle as we pass through a chiral symmetry restoring transition.

Next we repeated these measurements at $1/g^2 = 0.80$ in the $N_{f\text{latt}} = 3$ model in order to be closer to the model's continuum limit. At $1/g^2 = 0.80$ the $\mu = 0$ value of the fermion mass is $m_f = 0.295(3)$. On the basis of the analytic large- N_f results shown in Figs. 3,4 and 5, we anticipate that the transition will be harder to identify since finite size effects are more severe and smooth the transition considerably on a 16^3 lattice. We show the data for $1/g^2 = 0.80$ in Table III. It is organized just as Table II was. In Figs. 12 - 14 we show σ, ρ, ϵ and S plotted vs. μ . These figures show the same features as the large- N_f calculation, and indicate that the transition is in the vicinity of $\mu_c = 0.295(3)$. There is no evidence whatsoever for pathological behavior at $\mu = m_\pi/2 \approx 0.11(1)$. The transition is shown with greater clarity in the model's spectroscopy. In Fig. 15 we see that the dynamical fermion mass decreases, up to the expected finite size effects, linearly with μ and vanishes when μ becomes $0.25(5)$. Similarly, the pion mass is insensitive to μ until $\mu = 0.30(2)$, where it increases noticeably. We learn that the model's spectroscopy is a more sensitive guide to the chiral restoration transition than traditional bulk thermodynamic quantities. In light of our recent work on quenched QCD [4], this result comes as no surprise, but it reinforces the strategy we are taking in the four dimensional gauge model.

Next we turn to the $N_{f\text{latt}} = 1$ model to simulate a case where fluctuations are expected to be more significant, the number of flavors is more realistic and the large- N_f expansion may not be as good a guide. The $\mu = 0$ data is collected in Table IV. We notice, as plotted in Fig. 16, that the order parameter σ and dynamical fermion mass m_f disagree slightly deep in the broken symmetry phase, but are otherwise in good agreement. Since these two quantities are identical at large- N_f , we see signs of $1/N_f$ corrections here, but they are not numerically significant near the transition. We will investigate the theory at non-zero μ at both $1/g^2 = 0.60$ and 0.70 . The $1/g^2 = 0.60$ simulation is quite far in the broken phase and should be relatively decisive while the $1/g^2 = 0.70$ simulation will be more strongly affected by fluctuations. In Figs. 17 - 19 we show σ, ρ, ϵ and S plotted against μ

using the data of Table V. In this case the plots show only qualitative agreement with the predictions of the $1/N_f$ expansion at leading order; $O(1/N_f)$ corrections are numerically much more significant. We expect a transition near the value of the dynamical fermion mass at $1/g^2 = 0.60$, ie, $m_f = 0.475(5)$, and the figures are in fine agreement with that. In addition the fermion and pion masses, Fig. 20, show the transition almost as clearly and quantitatively as they did in the $N_{f\text{latt}} = 3$, $1/g^2 = 0.50$ case. Finally in Table VI and Figs. 21-24 we show the analogous quantities for the $N_{f\text{latt}} = 1$ theory at $1/g^2 = 0.70$. Although the bulk thermodynamic quantities experience considerable rounding, the results are consistent with a critical chemical potential $\mu_c = 0.32(1)$, as predicted by the value of the dynamical fermion mass at $1/g^2 = 0.70$. Once again, the spectroscopic quantities in Fig. 24 provide more quantitative information. All in all, the simulations are successful in each case and do not suffer from the pathologies affecting quenched QCD.

IV. CONCLUDING REMARKS

The success and clarity of these simulations shows that the Hybrid Monte Carlo algorithm (and hence presumably the closely related Hybrid Molecular Dynamics algorithm, suitable for values of N_f which are not a multiple of 4) are completely reliable for this class of fermion field theories in which there is a massless pion in the chiral limit. A chiral symmetry restoring phase transition, probably first order, is found for a critical value of the chemical potential μ . Screening length calculations proved to be particularly illuminating and the expected physics of chiral symmetry restoration at the critical chemical potential emerged. The spectroscopic data may well prove to be the most accurate means of determining the critical chemical potential on finite systems. The predictions of the large N_f expansion proved to be a good guide into the physics of these four fermi models even when N_f assumed modest values. Systematic effects are of the expected form, and we have no reason to suspect they could not be brought under complete control given sufficient computer time.

One of our primary motivations for this work was to narrow down the source of difficulties

in simulations of lattice QCD. We certainly have demonstrated that the presence of a massless pion in the theory's spectrum is *not* the source of those difficulties. By default it must be the complex nature of the QCD action at nonzero μ that is the culprit. The quenched version of QCD ignores the fermion determinant and this omission apparently amounts to a qualitative error when the chemical potential is larger than half the pion mass [4]. In four fermi models the fermion determinant is real and non-negative and the Euclidean theory has a probabilistic interpretation. In addition, the fermion propagator is well-behaved for all μ . These ingredients then allow the Hybrid algorithms to be successful in four fermi models despite being inapplicable for QCD. It may well be that Langevin algorithms [24] can simulate QCD directly at nonzero μ , but that is far from clear at this time (Langevin algorithms are known to correctly evaluate certain complex integrals, and certain physical systems with complex actions, but their successes and failures are difficult to anticipate in advance). It will probably require greater insight into the numerics of the complex fermion determinant before a truly trustworthy, first principles simulation of QCD in an environment rich in baryons is possible.

V. ACKNOWLEDGEMENTS

JBK is partially supported by the National Science Foundation under the grant NSF PHY92-00148. SK is supported by the U.S. Department of Energy, Contract No. W-30-109-ENG-38. SJH was supported in part by a CERN fellowship, and in part by a PPARC Advanced fellowship. The computer simulations were done on the Cray C90's at NERSC and PSC. We thank these computer centers for their help.

REFERENCES

- [1] I.M. Barbour, Nucl. Phys. **B**(Proc. Suppl.)**26**, 22 (1992).
- [2] I.M. Barbour, N.-E. Behilil, E. Dagotto, F. Karsch, A. Moreo, M.Stone and H.W. Wyld, Nucl. Phys. **B275** [FS17], 296 (1986).
- [3] C.T.H. Davies and E.G. Klepfish, Phys. Lett. **B256**, 68 (1991).
- [4] J.B. Kogut, M.-P. Lombardo and D.K. Sinclair, Illinois preprint ILL-(TH)-94-2 hep-lat/9401039 (to appear in Phys. Rev. D) (1994).
- [5] J. Vink, Nucl. Phys. **B323**, 399 (1989).
- [6] N. Bilić, K. Demeterfi and B. Petersson, Nucl. Phys. **B377**, 651 (1992).
- [7] E. Mendel, Nucl. Phys. **B387**, 485 (1992).
- [8] N. Bilić and K. Demeterfi, Phys. Lett. **B212**, 83 (1988).
- [9] P. Gibbs, Phys. Lett. **B182**, 369 (1986).
- [10] D.J. Gross and A. Neveu, Phys. Rev. **D20**, 3235 (1974).
- [11] B. Rosenstein, B.J. Warr and S.H. Park, Phys. Rep. **205**, 59 (1991).
- [12] B. Rosenstein, B.J. Warr and S.H. Park, Phys. Rev. **D39**, 3088 (1989).
- [13] S.J. Hands, A. Kocić and J.B. Kogut, Nucl. Phys. **B390**, 355 (1993).
- [14] S.J. Hands, A. Kocić and J.B. Kogut, Ann. Phys. **224**, 29 (1993).
- [15] H.-J. He, Y.-P. Yuang, Q. Wang and Y.-P. Yi, Phys. Rev. **D45**, 4610 (1992).
- [16] J.B. Kogut, H. Matsuoka, M. Stone, H.W. Wyld, S. Shenker, J. Shigemitsu and D.K. Sinclair, Nucl. Phys. **B225** [FS9], 93 (1983).
- [17] P. Hasenfratz and F. Karsch, Phys. Lett. **125B**, 308 (1983).
- [18] R.F. Dashen, S.-K. Ma and R. Rajamaran, Phys. Rev. **D11**, 1499 (1975).

- [19] F. Karsch, J.B. Kogut and H.W. Wyld, Nucl. Phys. **B280** [FS18], 289 (1987).
- [20] Y. Cohen, S. Elitzur and E. Rabinovici, Nucl. Phys. **B220**, 102 (1983).
- [21] S. Duane, A.D. Kennedy, B.J. Pendleton and D. Roweth, Phys. Lett. **B195**, 216 (1987).
- [22] S.J. Hands, A. Kocić, J.B. Kogut, R.L. Renken, D.K. Sinclair and K.C. Wang, Nucl. Phys. **B413**, 503 (1994).
- [23] S. Gottlieb, W. Liu, R.L. Renken, R.L. Sugar and D. Toussaint, Phys. Rev. **D38**, 2245 (1988).
- [24] G. Parisi, Phys. Lett. **131B**, 393 (1983), and references contained therein.

TABLES

TABLE I. $N_{f\text{latt}} = 3$ data on 16^3 lattice at $\mu = 0.0$. The columns give the coupling $1/g^2$, the fermion mass m_f , the pion mass m_π , the vacuum expectation value of the σ field σ , the action S .

$1/g^2$	m_f	m_π	σ	S
1.00	.102(2)	.22(1)	.094(2)	.363(2)
.95	.133(2)	.22(3)	.128(2)	.390(2)
.90	.182(2)	.19(3)	.176(3)	.428(2)
.85	.233(3)	.19(3)	.231(3)	.475(3)
.80	.295(3)	.21(3)	.294(3)	.535(3)
.75	.359(2)	.18(1)	.365(3)	.613(3)
.70	.430(2)	.18(2)	.438(4)	.707(3)
.65	.503(3)	.18(2)	.519(4)	.824(4)
.60	.573(3)	.18(1)	.604(4)	.969(5)
.55	—	—	.695(4)	1.14(1)
.50	.746(2)	.18(1)	.795(3)	1.36(1)

TABLE II. $N_{flatt} = 3$ data on 16^3 lattice at coupling $1/g^2 = 0.50$ for various chemical potentials μ . Same notation as Table I but ρ is the fermion density and ϵ is the energy density.

μ	m_f	m_π	ρ	σ	S	ϵ
.50	.236(1)	.188(2)	.00045(2)	.796(5)	1.36(1)	.217(1)
.60	.126(1)	.24(6)	.0069(4)	.783(4)	1.34(1)	.223(1)
.65	.060(4)	.21(1)	.0163(4)	.765(4)	1.31(1)	.232(1)
.70	0	.21(1)	.0905(4)	.586(4)	1.10(2)	.303(1)
.725		.40(2)	.230(1)	.131(4)	.79(2)	.426(1)
.75		.49(4)	.267(1)	.068(3)	.77(1)	.452(1)
.775		.55(8)	.299(2)	.050(3)	.75(1)	.475(1)
.80		.78(5)	.337(2)	.038(3)	.74(1)	.501(2)
.825		.78(5)	.374(2)	.026(2)	.74(1)	.526(2)
.85		—	.416(2)	.020(2)	.73(1)	.556(2)

TABLE III. Same as Table II except $1/g^2 = 0.80$.

μ	m_f	m_π	ρ	σ	S	ϵ
.15	.137(2)	.22(1)	.0026(2)	.287(1)	.532(1)	.303(1)
.20	.075(3)	.20(1)	.0047(1)	.274(1)	.525(1)	.305(1)
.225	.041(4)	.26(2)	.0078(1)	.262(2)	.518(1)	.308(1)
.25	.010(5)	.22(1)	.0120(7)	.245(1)	.511(1)	.310(1)
.275	0	.24(1)	.0162(6)	.220(1)	.501(1)	.314(1)
.30		.25(2)	.0220(3)	.190(1)	.490(1)	.319(1)
.325		.28(3)	.0288(2)	.160(1)	.480(1)	.323(1)
.35		.30(3)	.0375(4)	.129(1)	.472(1)	.329(1)
.40		.35(3)	.056(1)	.083(1)	.461(1)	.339(1)
.50		.65(5)	.099(1)	.042(1)	.452(1)	.360(1)

TABLE IV. Same as Table I except $N_{flatt} = 1$.

$1/g^2$	m_f	m_π	σ	S	ϵ
1.00	.070(1)	.25(5)	.064(2)	1.063(1)	.314(1)
.95	.075(5)	.22(3)	.078(2)	1.121(1)	.313(1)
.90	.105(2)	.23(3)	.106(5)	1.193(1)	.309(1)
.85	.14(2)	.20(2)	.141(5)	1.277(1)	.305(1)
.80	.192(4)	.21(2)	.200(7)	1.381(2)	.298(2)
.70	.32(1)	.15(2)	.336(9)	1.655(2)	.280(2)
.60	.475(5)	.26(5)	.511(12)	2.065(2)	.253(3)
.50	.650(5)	.15(1)	.706(15)	2.675(2)	.220(3)

TABLE V. Same as Table II except $N_{flatt} = 1$ and $1/g^2 = 0.60$.

μ	m_f	m_π	σ	ρ	S	ϵ
.30	.173(1)	.15(2)	.498(2)	.00133(57)	2.062(1)	.255(1)
.35	.116(2)	.20(5)	.491(2)	.00432(19)	2.055(1)	.257(1)
.40	.046(2)	.15(2)	.470(2)	.0104(3)	2.038(1)	.252(1)
.425	0	—	.439(4)	.0171(4)	2.018(2)	.268(1)
.45		.19(2)	.373(15)	.0312(3)	1.977(4)	.281(1)
.475		.22(2)	.259(15)	.0541(8)	1.924(3)	.300(1)
.4875		.25(3)	.206(15)	.0644(3)	1.904(2)	.308(1)
.50		.30(2)	.178(5)	.0731(5)	1.890(2)	.313(1)
.525		.30(2)	.124(3)	.0892(4)	1.871(1)	.325(1)
.55		.36(3)	.091(5)	.1034(5)	1.859(1)	.333(1)
.60		.52(4)	.060(7)	.1310(7)	1.843(1)	.350(1)

TABLE VI. Same as Table V except $1/g^2 = 0.070$.

μ	m_f	m_π	σ	ρ	S	ϵ
.15	.164(1)	.22(1)	.331(1)	.00067(33)	1.65(1)	.281(1)
.20	.113(5)	.22(1)	.324(1)	.00247(64)	1.65(1)	.282(1)
.225	.085(5)	.21(1)	.315(1)	.00468(9)	1.64(1)	.283(1)
.25	.040(8)	.22(2)	.301(1)	.00689(43)	1.63(1)	.284(1)
.275	—	.24(1)	.273(3)	.0102(3)	1.62(1)	.289(1)
.30	0	.26(2)	.235(7)	.0175(4)	1.61(1)	.294(1)
.325		.30(1)	.195(5)	.0235(7)	1.60(1)	.299(1)
.35		.25(2)	.162(7)	.0309(6)	1.59(1)	.304(1)
.40		.38(1)	.107(7)	.0490(3)	1.58(1)	.314(1)
.50		.50(5)	.052(3)	.0898(3)	1.56(1)	.335(1)

Figure Captions

Figure 1: Plot of $\langle\sigma\rangle$ versus $1/g^2$ at $\mu = 0$ evaluated using the gap equation (2.14) on a 16^3 lattice for three different bare fermion masses m .

Figure 2: Gap equation prediction of $\langle\sigma\rangle$ versus μ at $1/g^2 = 0.5$ for three different m .

Figure 3: Gap equation prediction of $\langle\sigma\rangle$ versus μ for $m = 0.01$ at four different $1/g^2$.

Figure 4: Gap equation prediction of number density ρ versus μ at three different $1/g^2$, plus the continuum free-field prediction.

Figure 5: Gap equation prediction of energy density ϵ versus μ at three different $1/g^2$.

Figure 6: Simulation results for σ versus $1/g^2$ at $\mu = 0$ using $N_{\text{flatt}} = 3$ and $m = 0.01$. Also shown is the gap equation prediction of Fig. 1.

Figure 7: Simulation results for σ versus μ at $1/g^2 = 0.5$ using $N_{\text{flatt}} = 3$. Also shown is the gap equation prediction of Fig. 3.

Figure 8: Simulation results for σ versus m at $1/g^2 = 0.5$ and $\mu = 0.5$ using $N_{\text{flatt}} = 3$.

Figure 9: Simulation results for ρ and ϵ versus μ at $1/g^2 = 0.5$ using $N_{\text{flatt}} = 3$.

Figure 10: Simulation results for action S versus μ at $1/g^2 = 0.5$ using $N_{\text{flatt}} = 3$.

Figure 11: Simulation results for fermion mass m_f and pion mass m_π at $1/g^2 = 0.5$ using $N_{\text{flatt}} = 3$.

Figure 12: Same as Fig. 7 except $1/g^2 = 0.8$.

Figure 13: Same as Fig. 9 except $1/g^2 = 0.8$.

Figure 14: Same as Fig. 10 except $1/g^2 = 0.8$.

Figure 15: Same as Fig. 11 except $1/g^2 = 0.8$.

Figure 16: Same as Fig. 6 except $N_{\text{flatt}} = 1$. Also shown is fermion mass m_f .

Figure 17: Same as Fig. 7 except $N_{\text{flatt}} = 1$ and $1/g^2 = 0.6$.

Figure 18: Same as Fig. 9 except $N_{\text{flatt}} = 1$ and $1/g^2 = 0.6$.

Figure 19: Same as Fig. 10 except $N_{\text{flatt}} = 1$ and $1/g^2 = 0.6$.

Figure 20: Same as Fig. 11 except $N_{\text{flatt}} = 1$ and $1/g^2 = 0.6$.

Figure 21: Same as Fig. 17 except $1/g^2 = 0.7$.

Figure 22: Same as Fig. 18 except $1/g^2 = 0.7$.

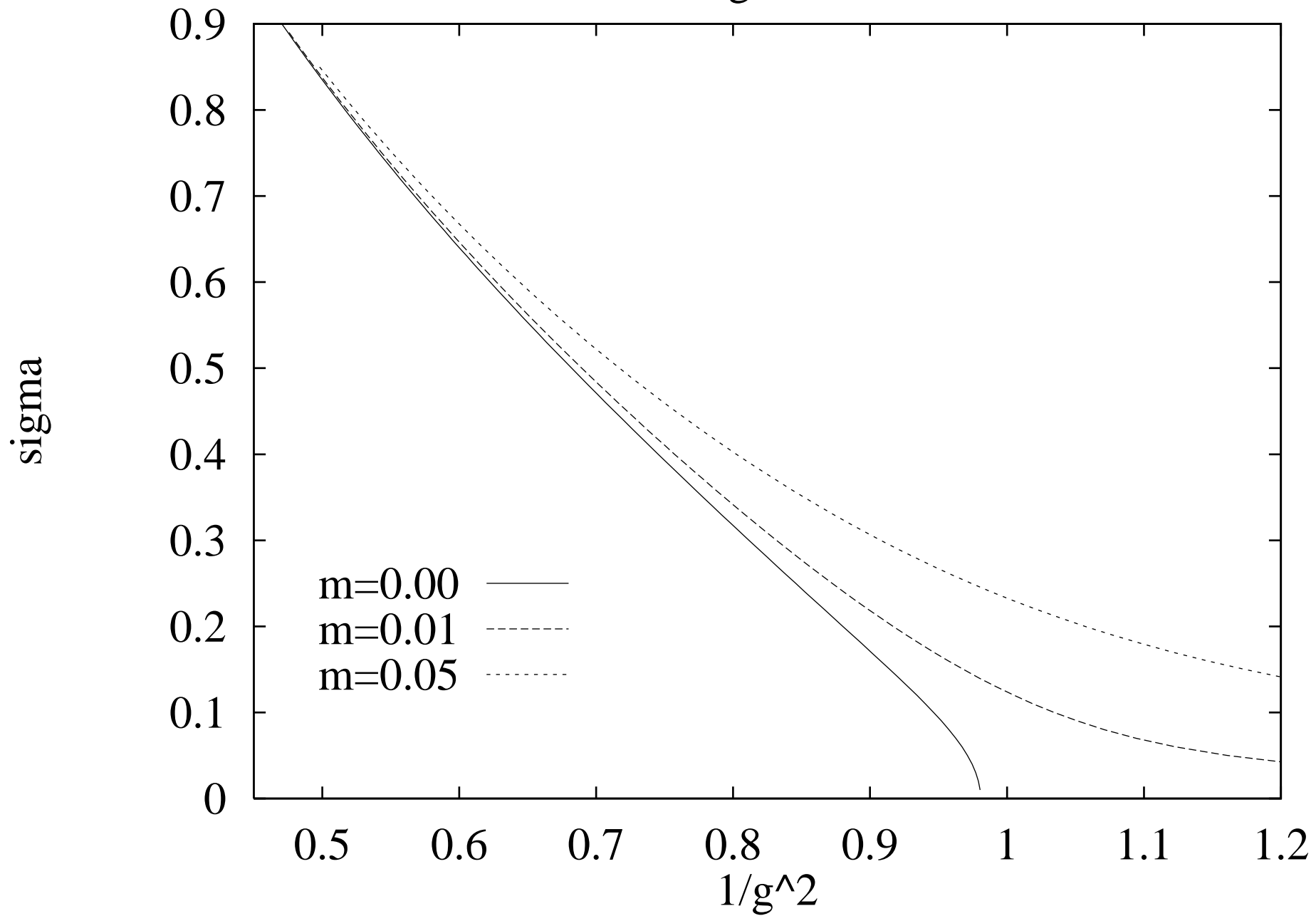
Figure 23: Same as Fig. 19 except $1/g^2 = 0.7$.

Figure 24: Same as Fig. 20 except $1/g^2 = 0.7$.

This figure "fig1-1.png" is available in "png" format from:

<http://arxiv.org/ps/hep-lat/9501037v1>

Figure 1



This figure "fig2-1.png" is available in "png" format from:

<http://arxiv.org/ps/hep-lat/9501037v1>

This figure "fig3-1.png" is available in "png" format from:

<http://arxiv.org/ps/hep-lat/9501037v1>

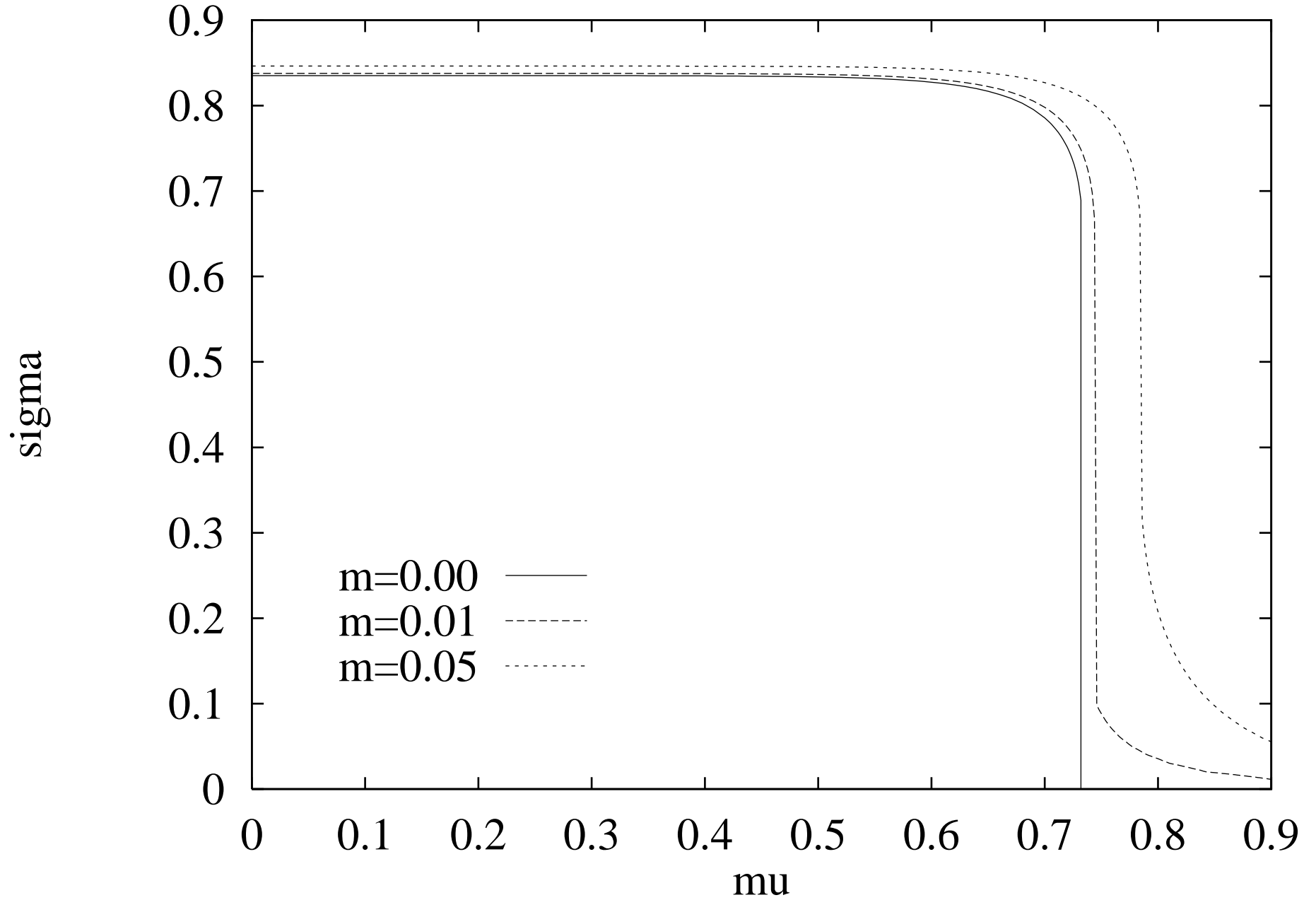
This figure "fig1-2.png" is available in "png" format from:

<http://arxiv.org/ps/hep-lat/9501037v1>

This figure "fig2-2.png" is available in "png" format from:

<http://arxiv.org/ps/hep-lat/9501037v1>

Figure 2



This figure "fig3-2.png" is available in "png" format from:

<http://arxiv.org/ps/hep-lat/9501037v1>

This figure "fig1-3.png" is available in "png" format from:

<http://arxiv.org/ps/hep-lat/9501037v1>

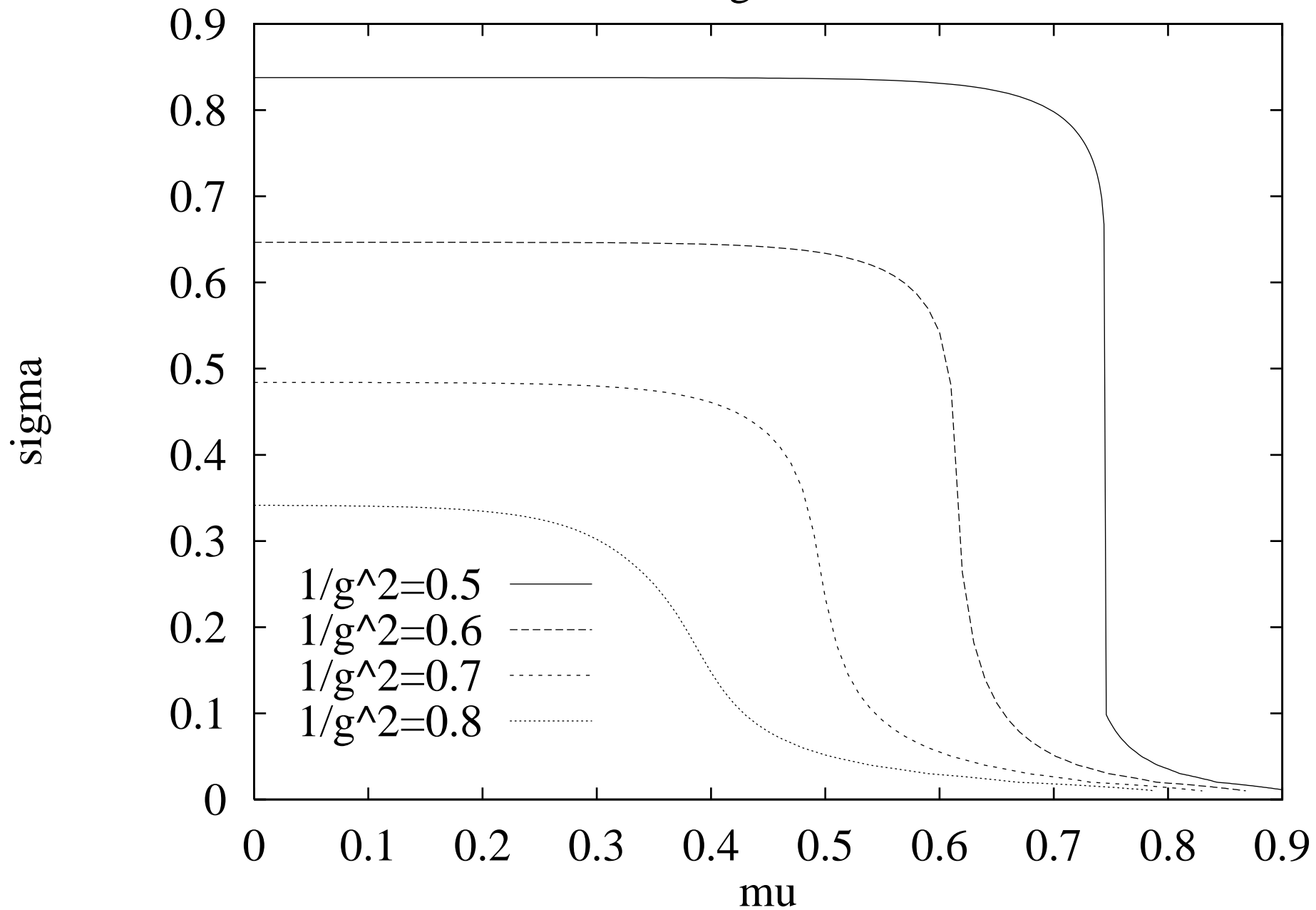
This figure "fig2-3.png" is available in "png" format from:

<http://arxiv.org/ps/hep-lat/9501037v1>

This figure "fig3-3.png" is available in "png" format from:

<http://arxiv.org/ps/hep-lat/9501037v1>

Figure 3



This figure "fig1-4.png" is available in "png" format from:

<http://arxiv.org/ps/hep-lat/9501037v1>

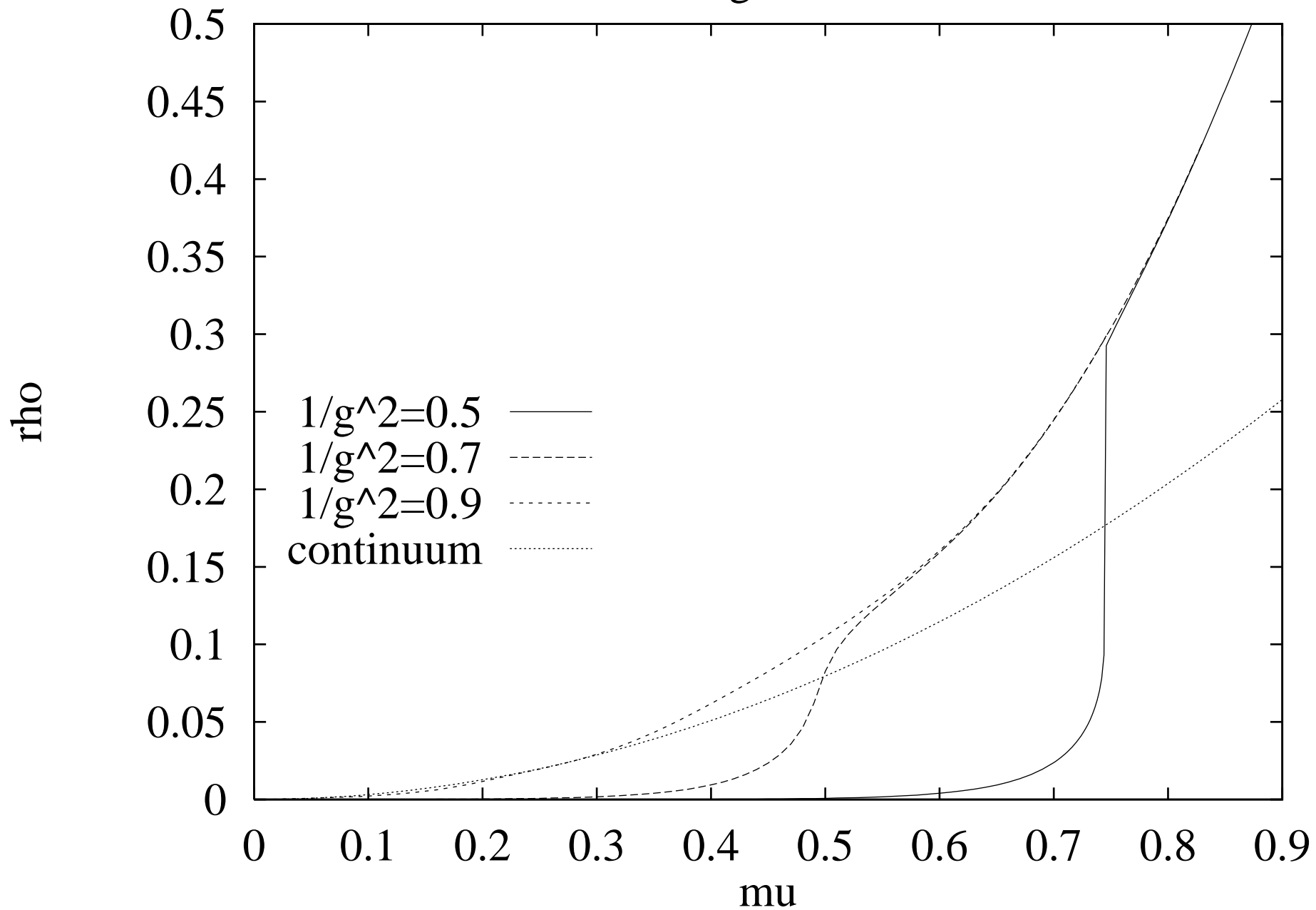
This figure "fig2-4.png" is available in "png" format from:

<http://arxiv.org/ps/hep-lat/9501037v1>

This figure "fig3-4.png" is available in "png" format from:

<http://arxiv.org/ps/hep-lat/9501037v1>

Figure 4



This figure "fig1-5.png" is available in "png" format from:

<http://arxiv.org/ps/hep-lat/9501037v1>

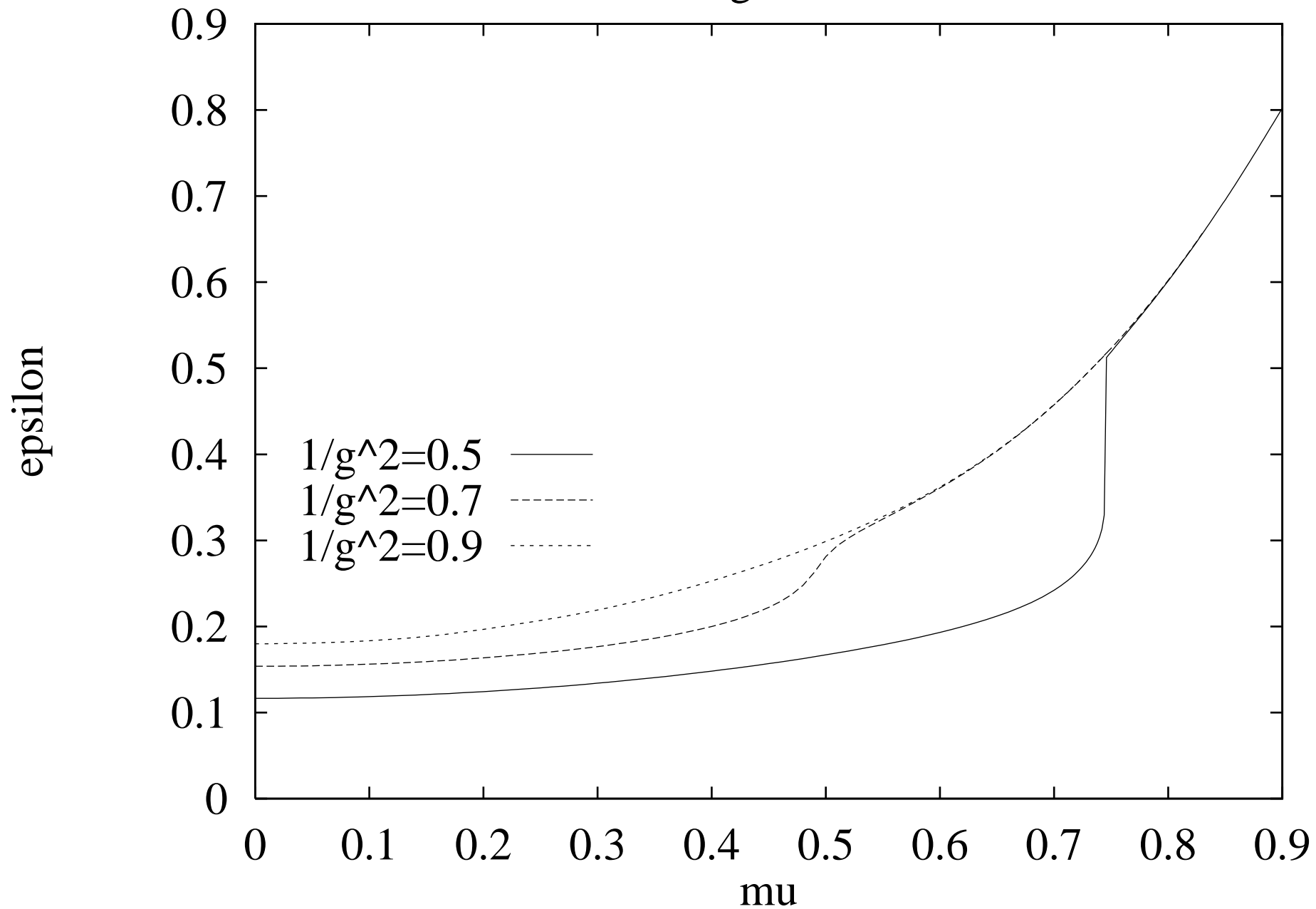
This figure "fig2-5.png" is available in "png" format from:

<http://arxiv.org/ps/hep-lat/9501037v1>

This figure "fig3-5.png" is available in "png" format from:

<http://arxiv.org/ps/hep-lat/9501037v1>

Figure 5



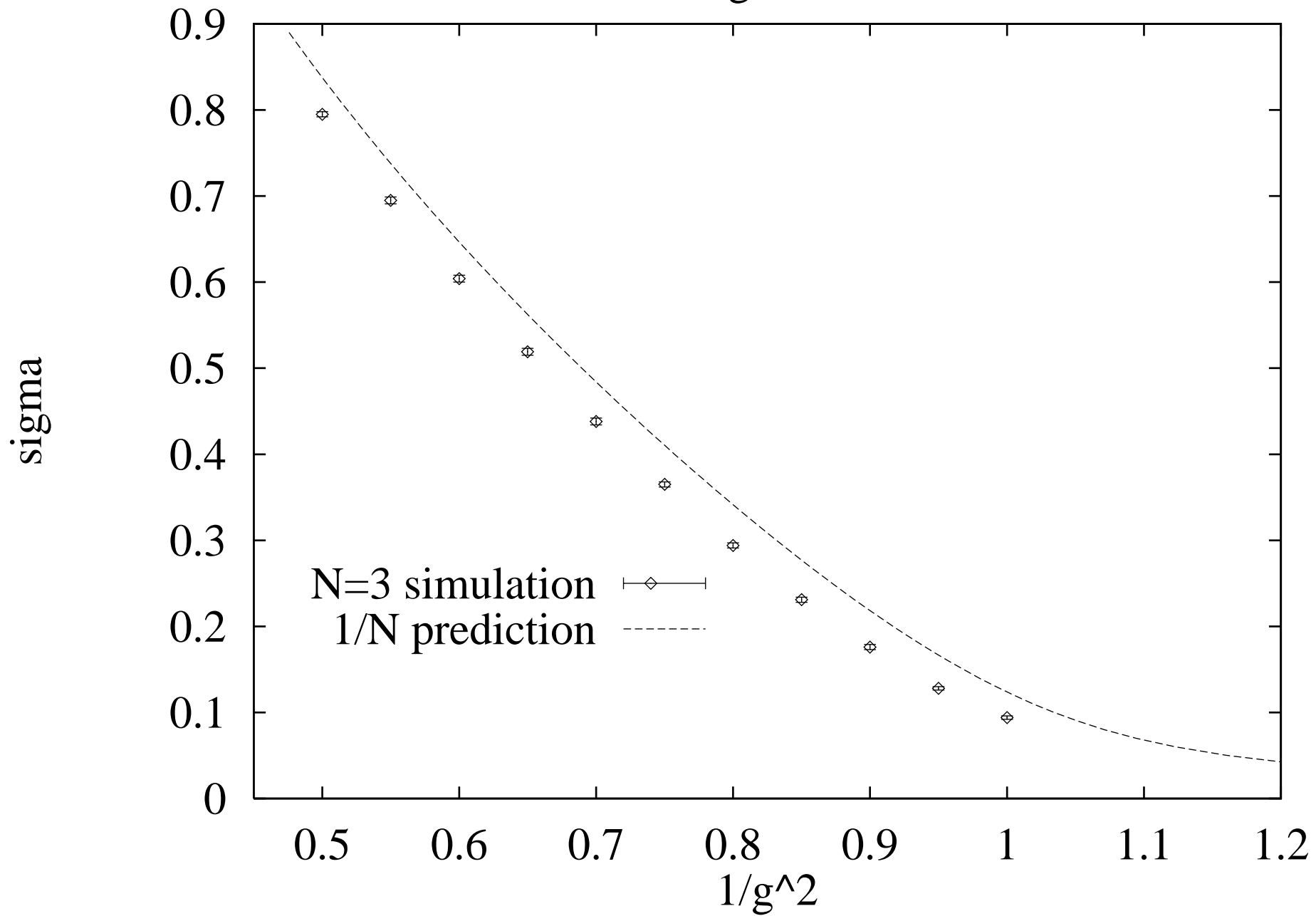
This figure "fig1-6.png" is available in "png" format from:

<http://arxiv.org/ps/hep-lat/9501037v1>

This figure "fig2-6.png" is available in "png" format from:

<http://arxiv.org/ps/hep-lat/9501037v1>

Figure 6



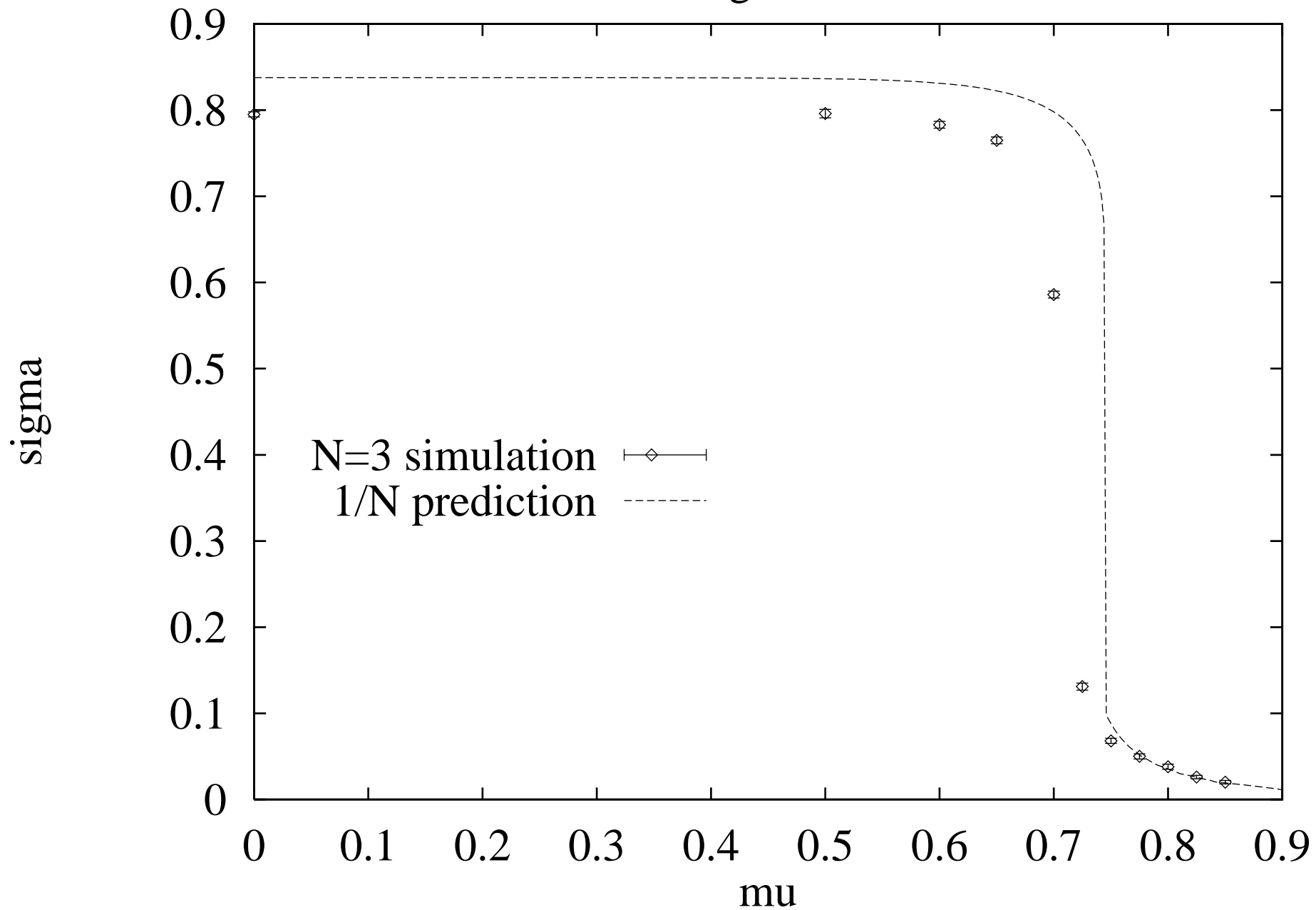
This figure "fig1-7.png" is available in "png" format from:

<http://arxiv.org/ps/hep-lat/9501037v1>

This figure "fig2-7.png" is available in "png" format from:

<http://arxiv.org/ps/hep-lat/9501037v1>

Figure 7



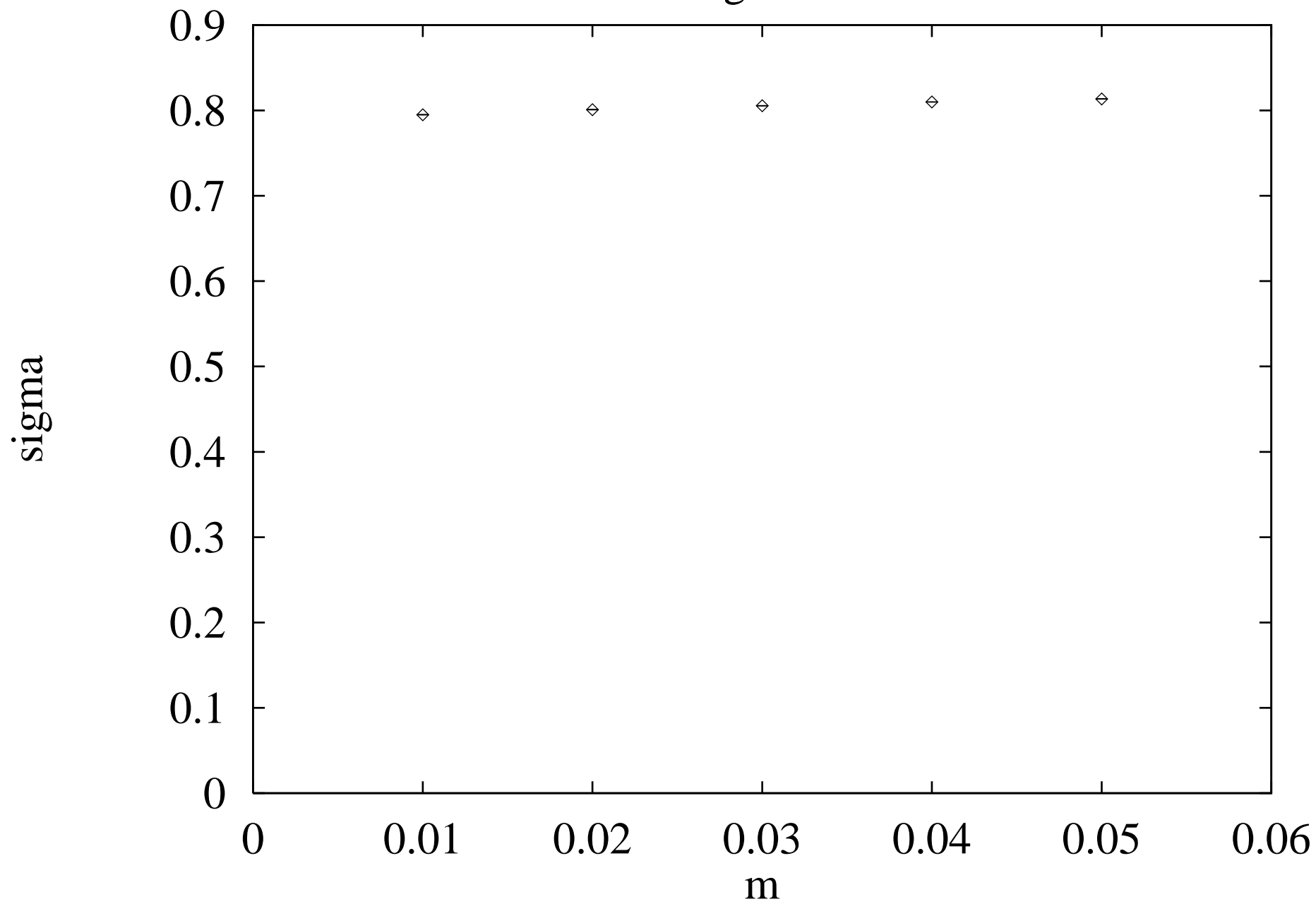
This figure "fig1-8.png" is available in "png" format from:

<http://arxiv.org/ps/hep-lat/9501037v1>

This figure "fig2-8.png" is available in "png" format from:

<http://arxiv.org/ps/hep-lat/9501037v1>

Figure 8



This figure "fig1-9.png" is available in "png" format from:

<http://arxiv.org/ps/hep-lat/9501037v1>

This figure "fig2-9.png" is available in "png" format from:

<http://arxiv.org/ps/hep-lat/9501037v1>

Figure 9

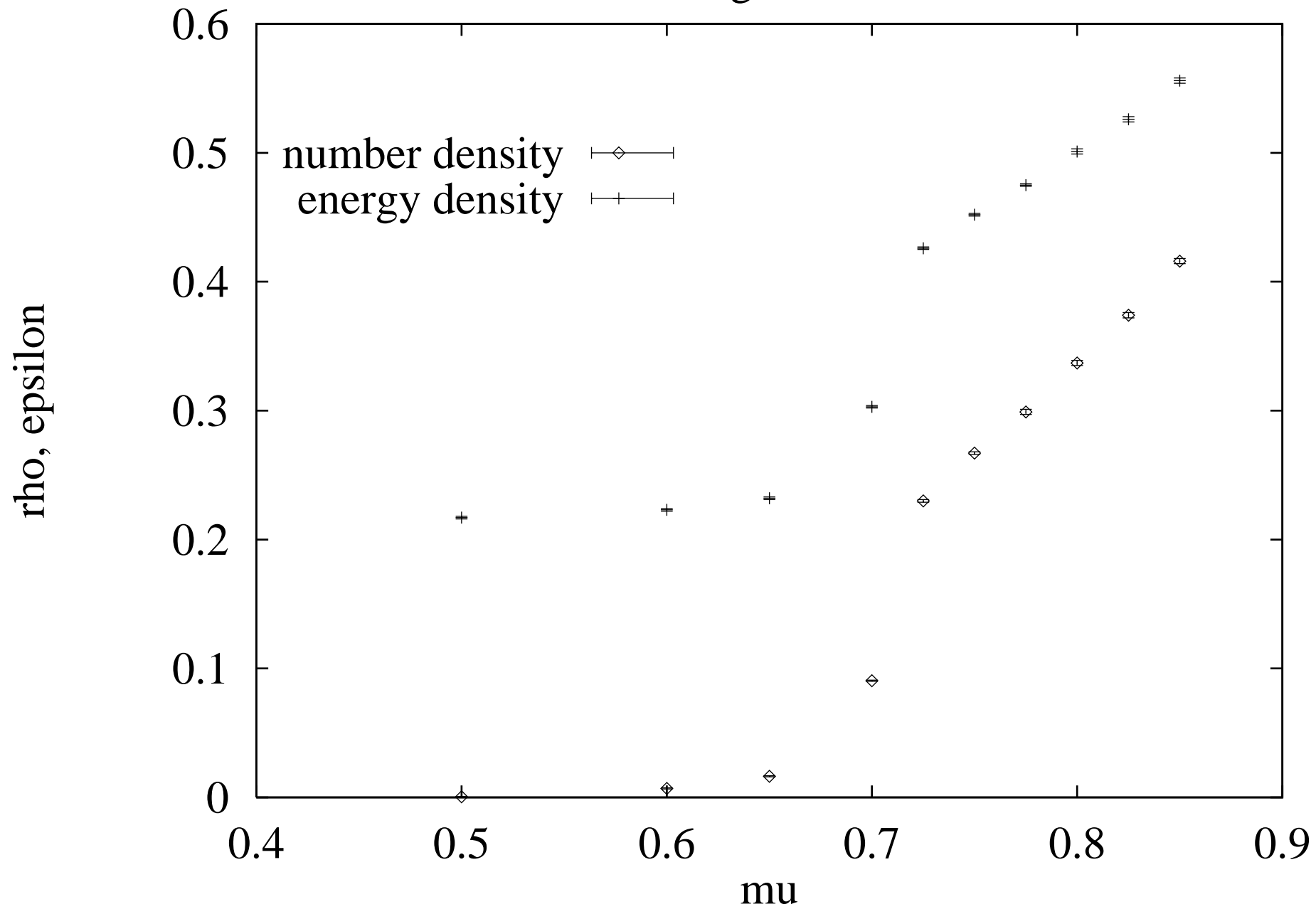
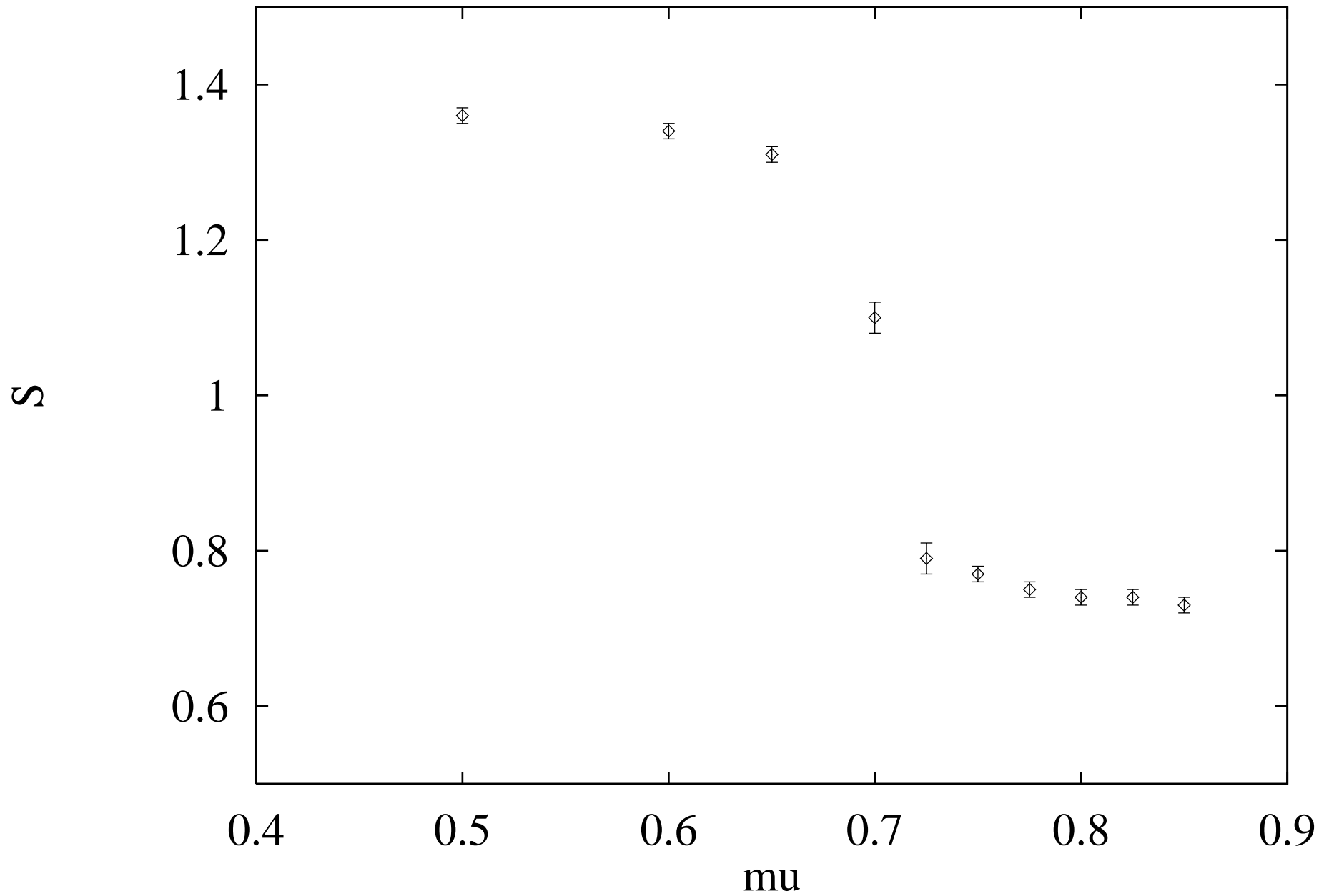


Figure 10



This figure "fig2-10.png" is available in "png" format from:

<http://arxiv.org/ps/hep-lat/9501037v1>

Figure 11

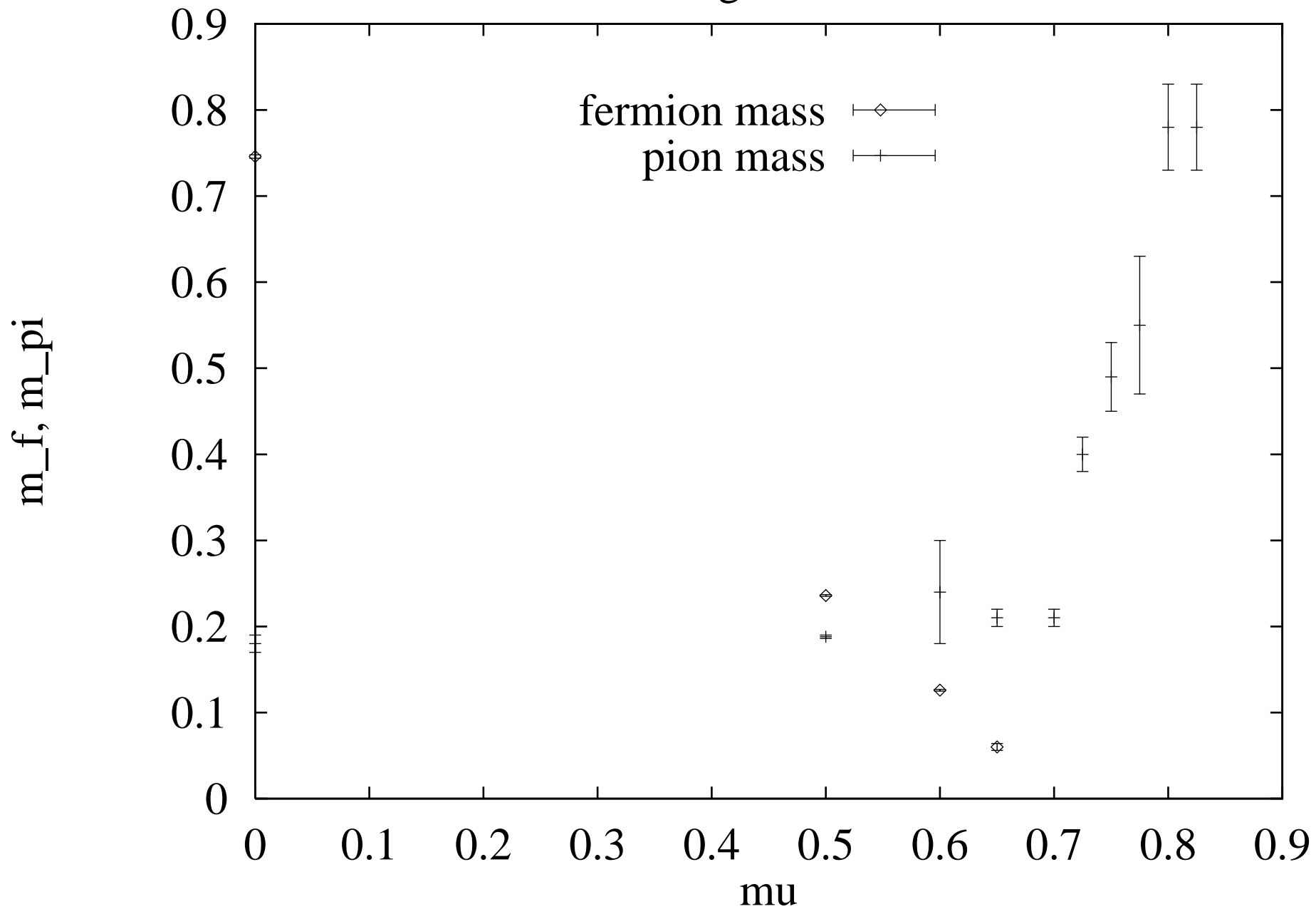


Figure 12

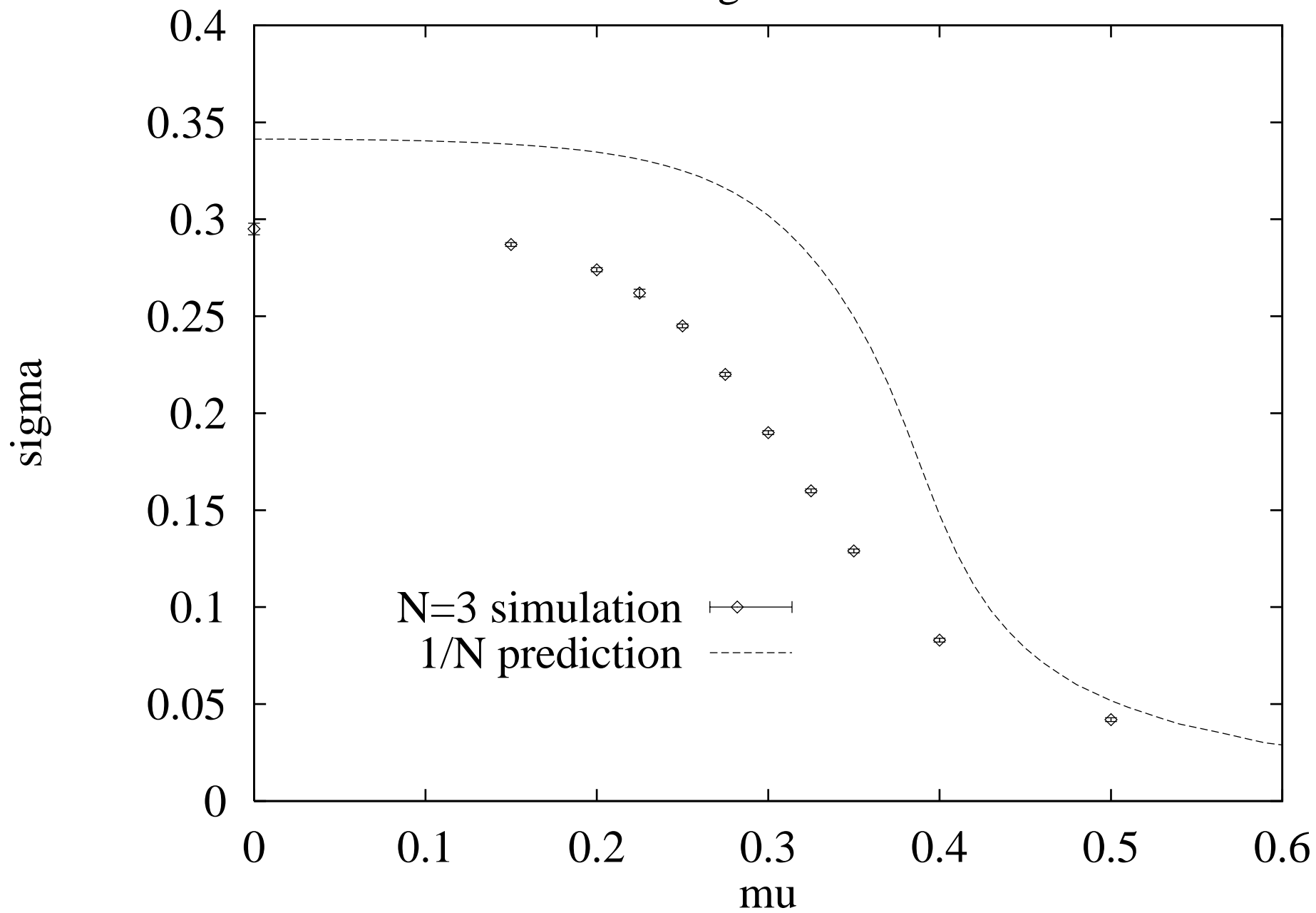


Figure 13

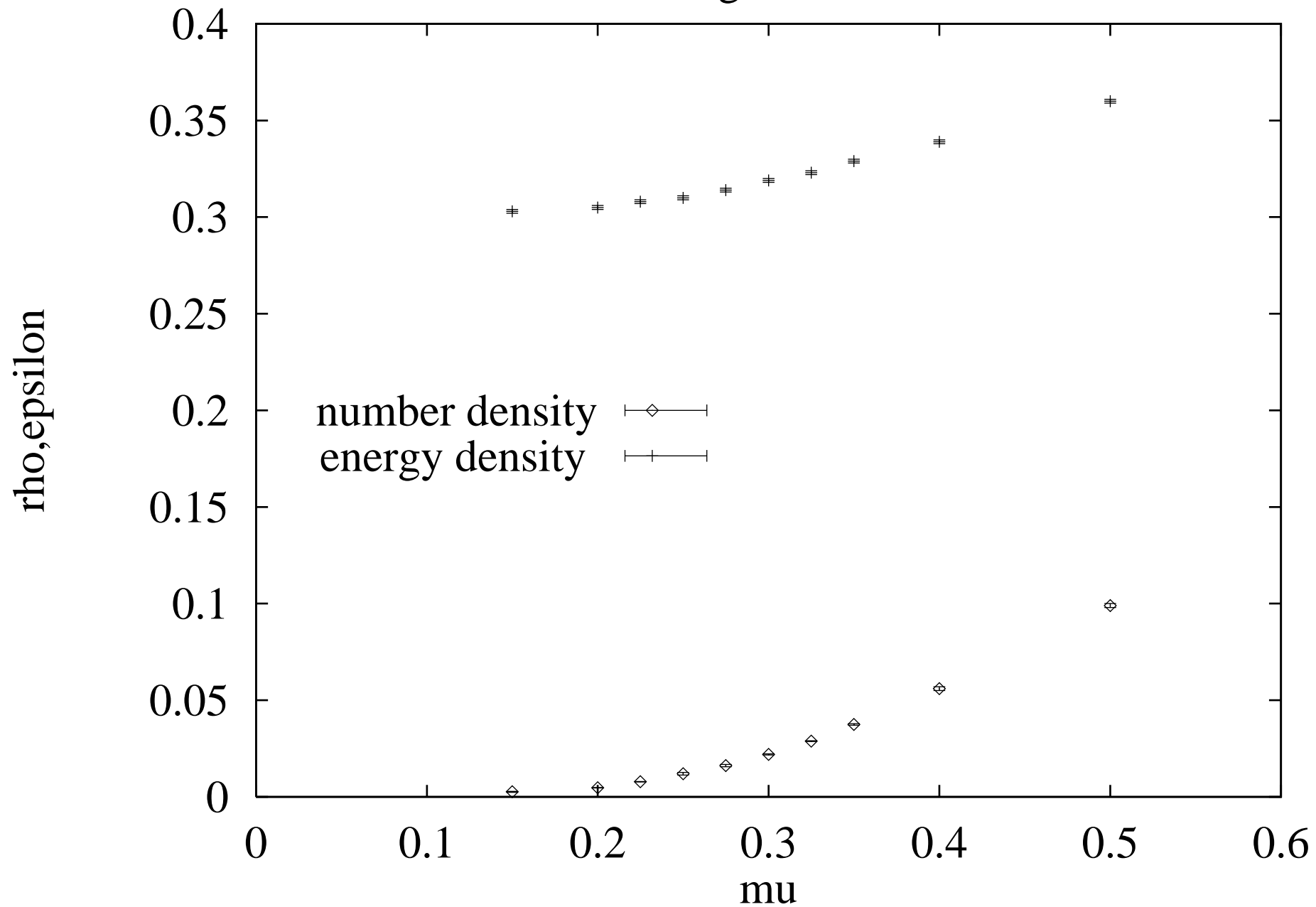


Figure 14

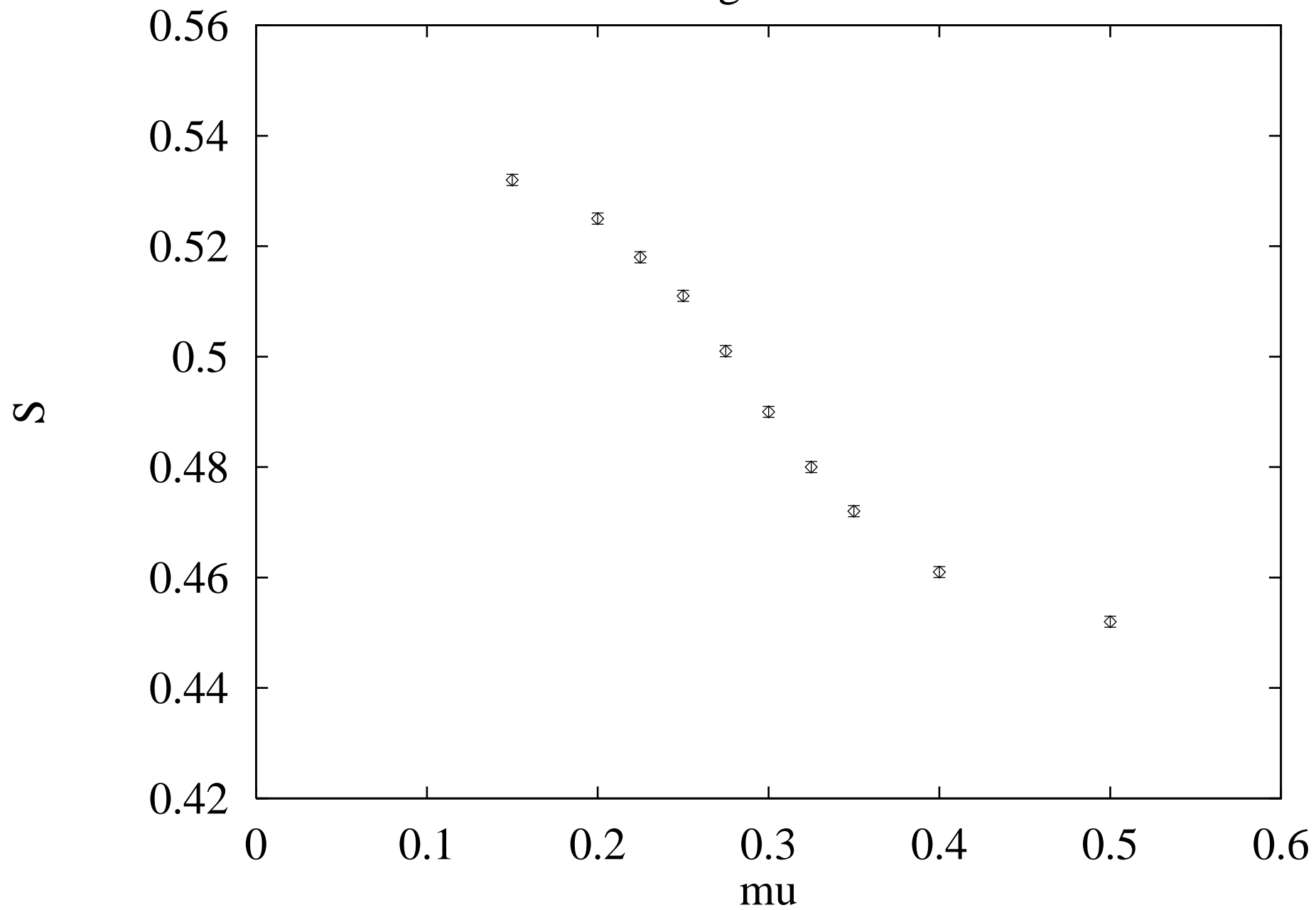


Figure 15

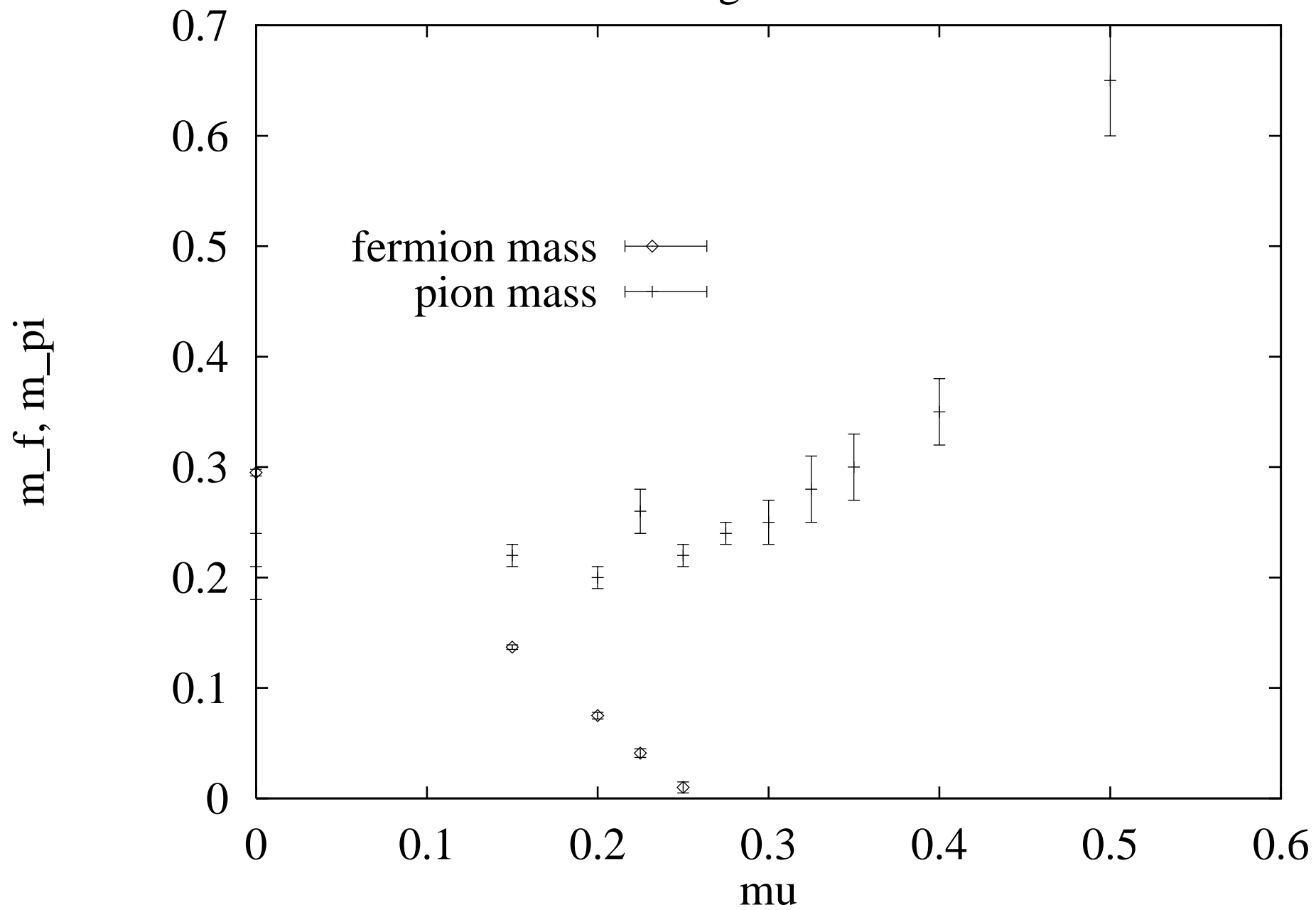


Figure 16

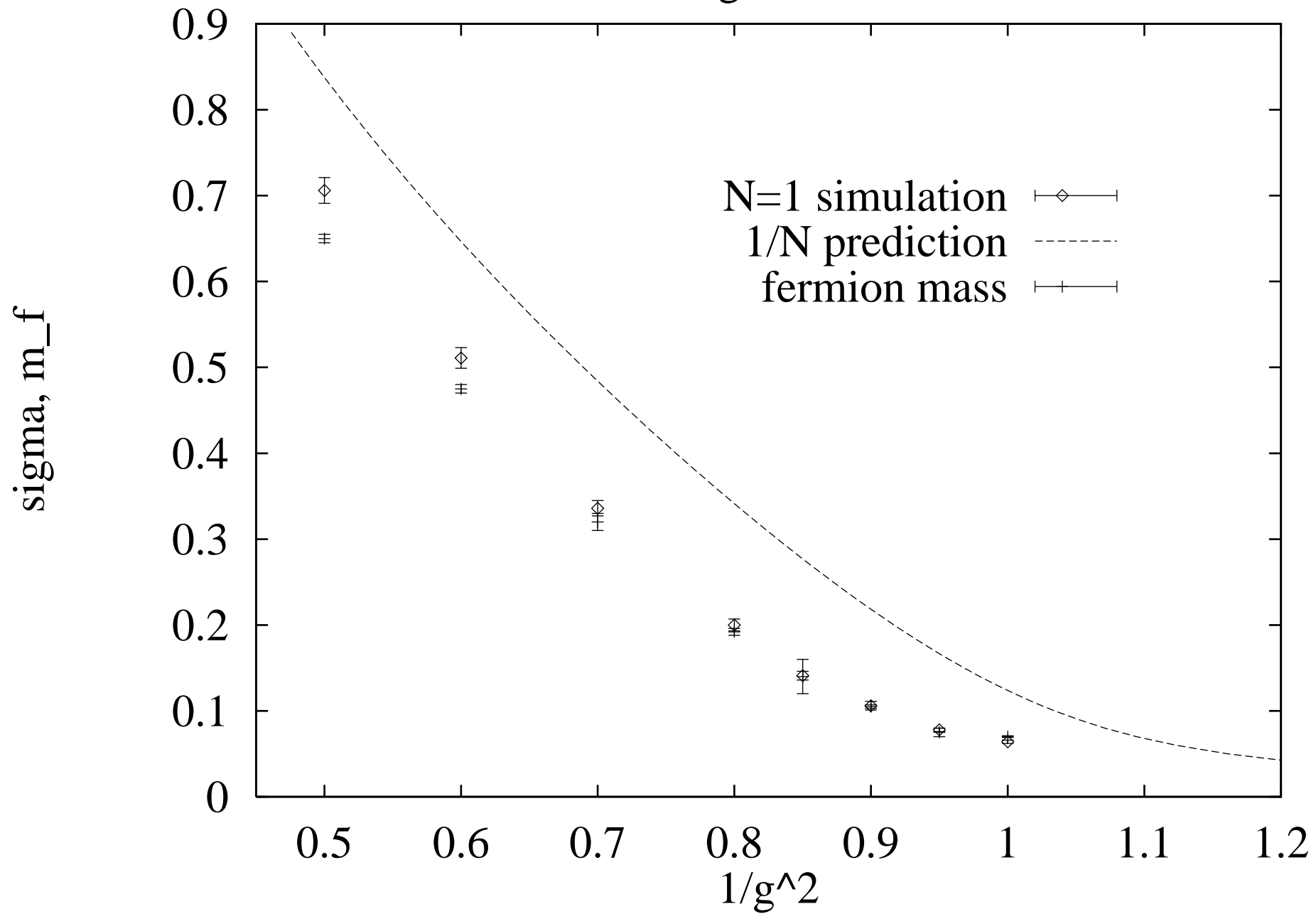


Figure 17

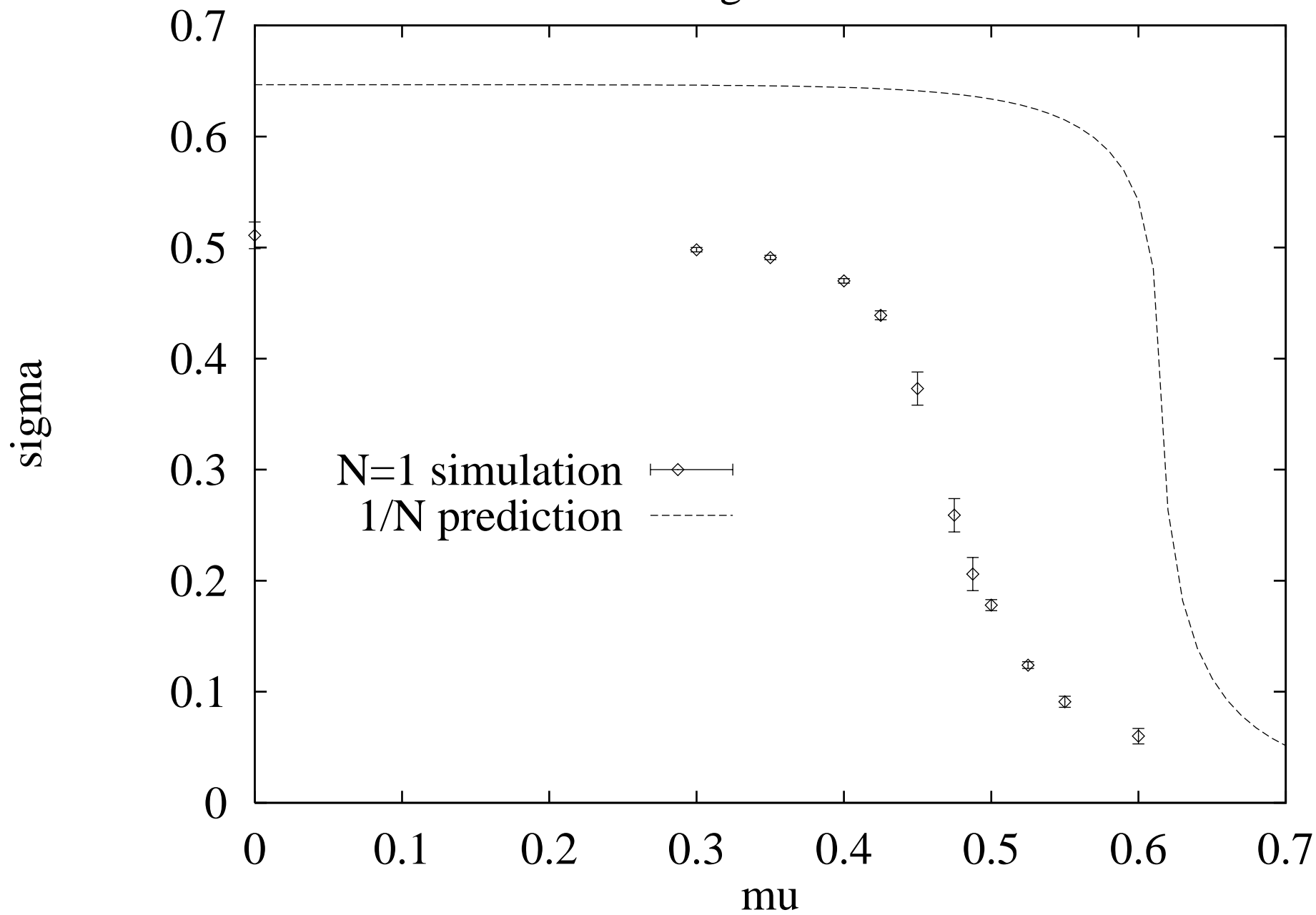


Figure 18

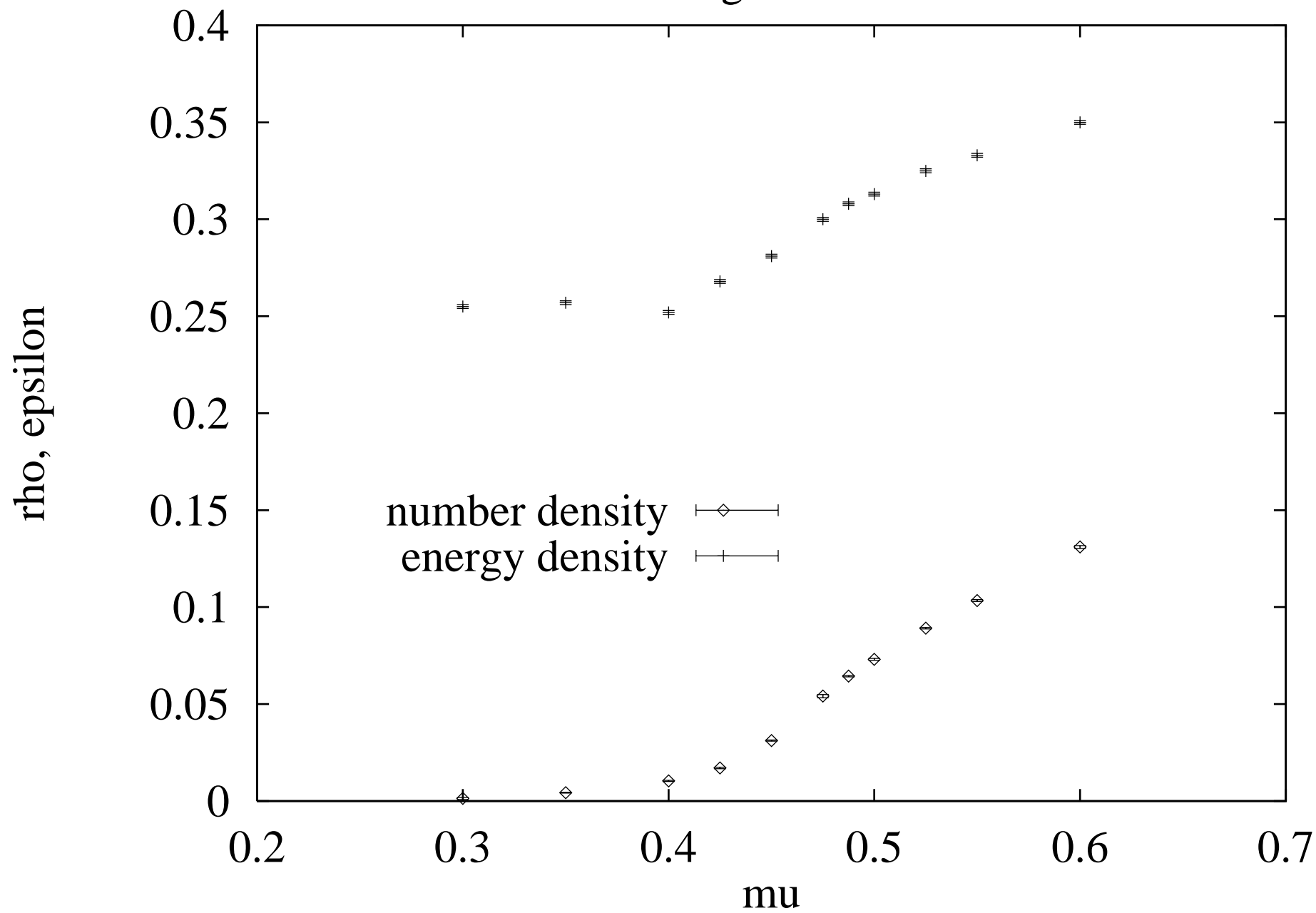


Figure 19

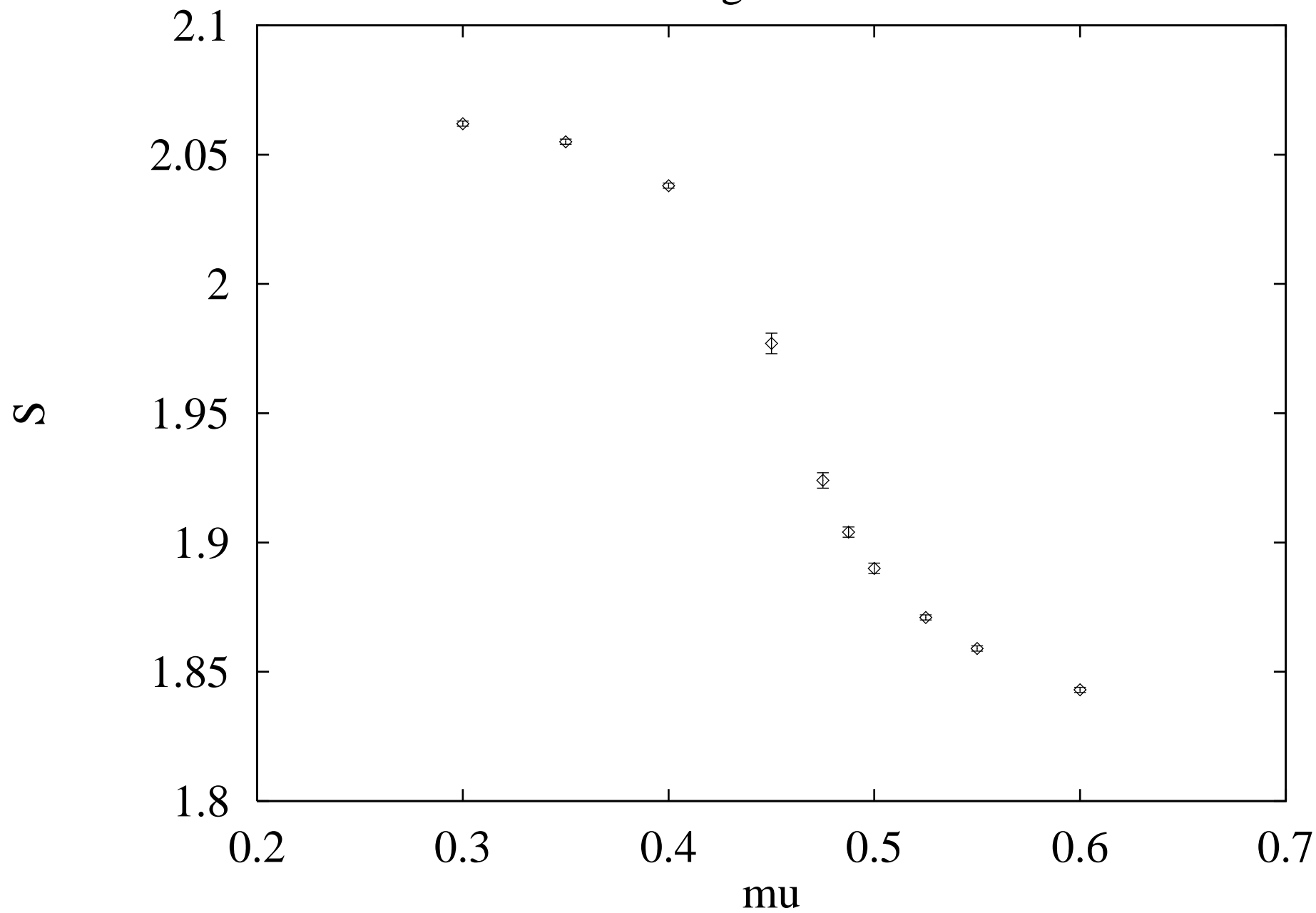


Figure 20

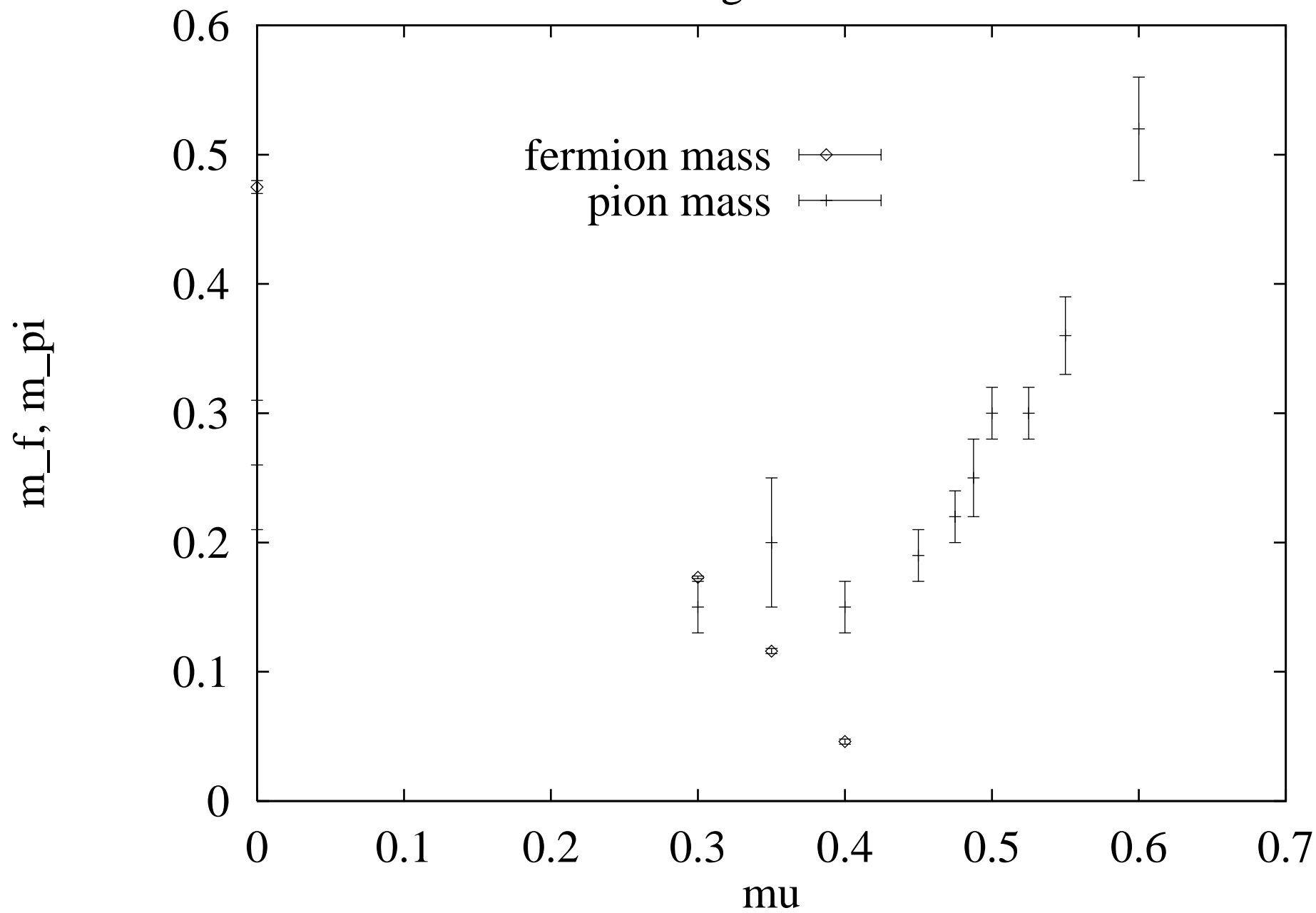


Figure 21

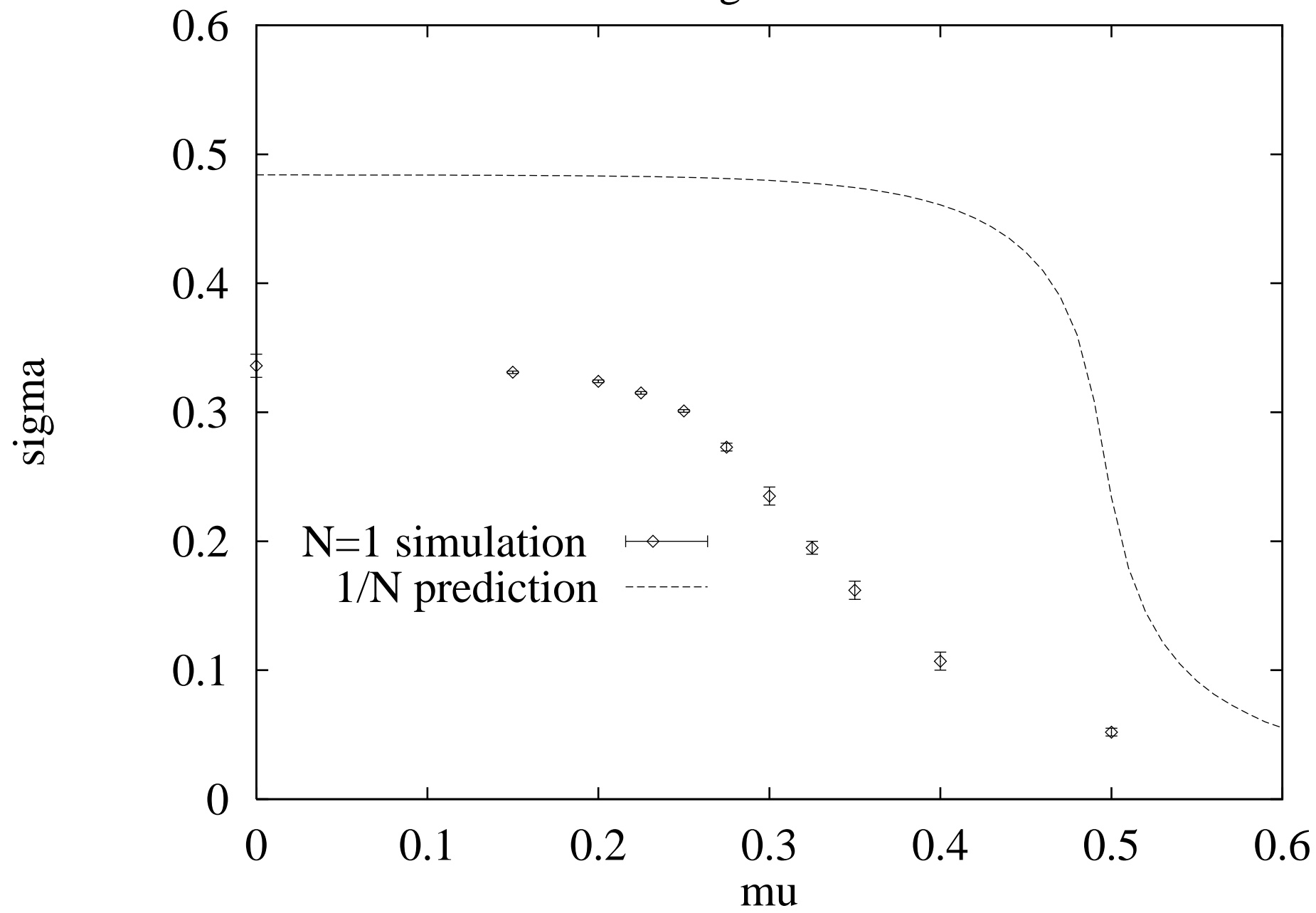


Figure 22

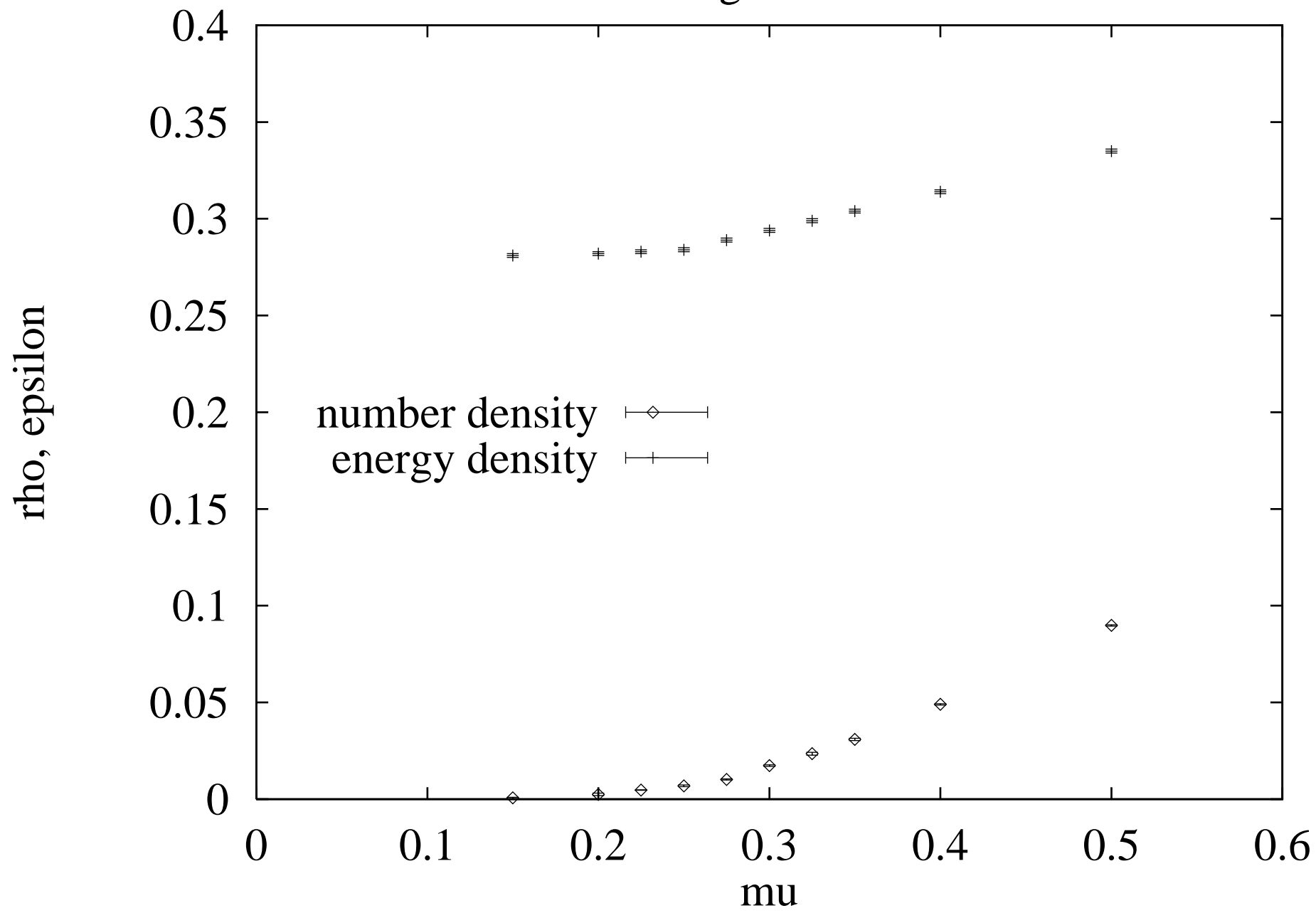


Figure 23

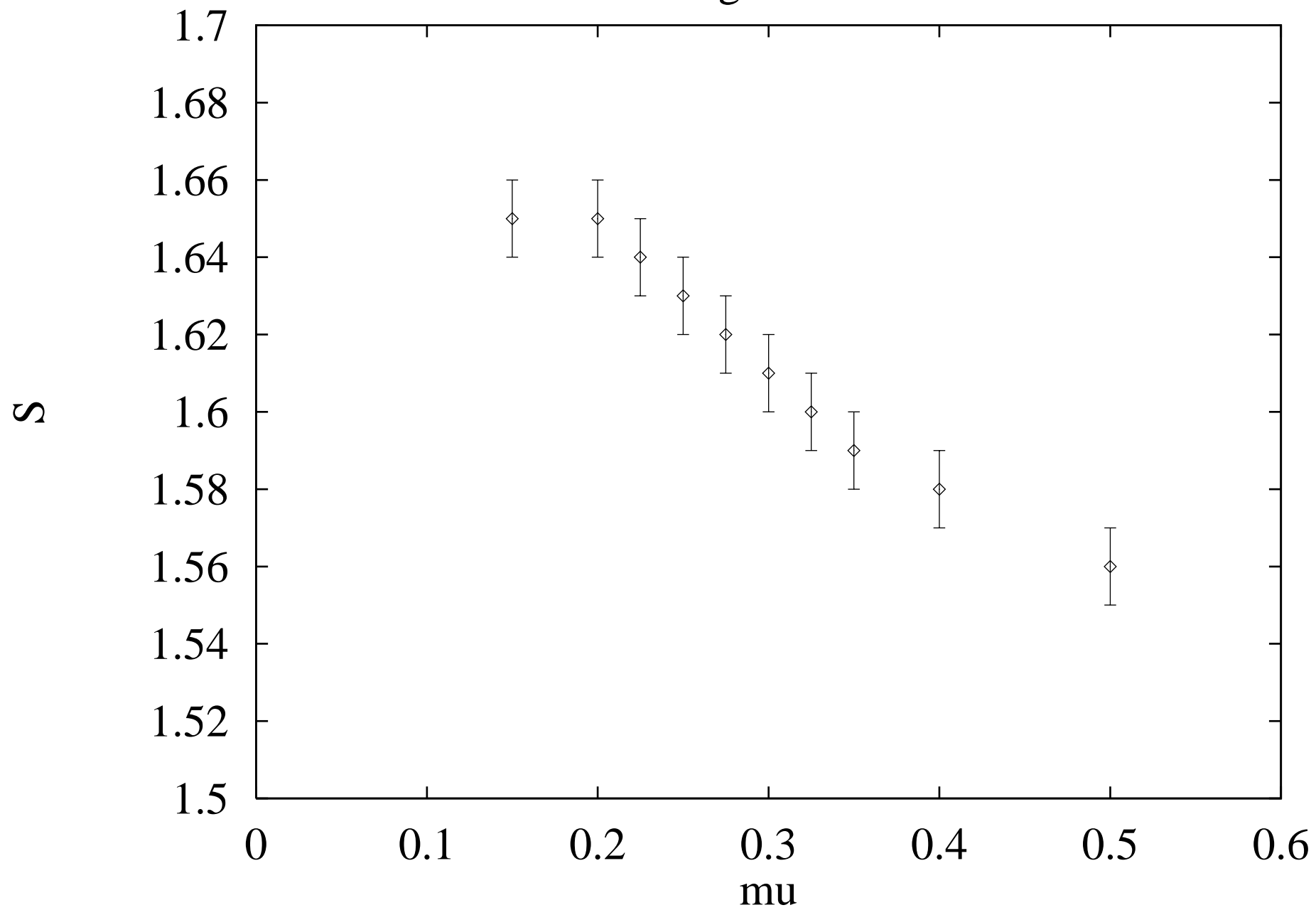


Figure 24

